Geophysical Journal International

Geophys. J. Int. (2022) **228,** 2073–2091
Advance Access publication 2021 October 05
GJI Geomagnetism, rock magnetism and palaeomagnetism

https://doi.org/10.1093/gji/ggab402

Remagnetization of the Jurassic limestones in the Zaduo area, Eastern Qiangtang Terrane (Tibetan Plateau, China): implications for the India–Eurasia collision

Qiang Fu [1,2,3] Maodu Yan,[1] Mark J. Dekkers,[3] Chong Guan,[4] Liang Yu,[1,2] Wanlong Xu,[1,2] Bingshuai Li,[5] Zhantao Feng,[6] Zunbo Xu,[1,2] Miaomiao Shen[1] and Dawen Zhang[7]

[1]*State Key Laboratory of Tibetan Plateau Earth System, Resources and Environment (TPESRE), Institute of Tibetan Plateau Research, Chinese Academy of Sciences, Beijing* 100101*, China. E-mail: maoduyan@itpcas.ac.cn*
[2]*College of Earth Sciences, University of Chinese Academy of Sciences, Beijing* 100049*, China*
[3]*Department of Earth Sciences, Paleomagnetic Laboratory 'Fort Hoofddijk', Utrecht University, Budapestlaan* 17, 3584 *CD Utrecht, The Netherlands*
[4]*Xi'an Center of Geological Survey (Northwest China Center of Geoscience Innovation), China Geological Survey, Xi'an* 710054*, China*
[5]*School of Earth Sciences, East China University of Technology, Nanchang* 330013*, China*
[6]*MOE Key Laboratory of Western China's Environmental Systems, College of Earth and Environmental Sciences, Lanzhou University, Lanzhou* 730000*, China*
[7]*School of Tourism, Resources and Environment, Zaozhuang University, Zaozhuang* 277160*, China*

Accepted 2021 September 30. Received 2021 September 23; in original form 2021 August 9

SUMMARY

A series of terranes were accreted to Eurasia in the region of what is now the Tibetan Plateau, including the Qaidam-Qilian, the Songpan-Ganzi, the Qiangtang, the Lhasa and the Tethyan Himalaya terranes. The drift history of the Qiangtang Terrane and the timing of the Lhasa–Qiangtang collision are controversial. To contribute to this topic, here, we palaeomagnetically investigate the Middle-Upper Jurassic limestones of the Yanshiping group in the Zaduo area (32.5°N, 95.2°E), in the Estern Qiangtang Terrane. Twelve sites (133 samples) were processed. A major challenge in palaeomagnetism is the possibility of remagnetization that interferes with palaeogeographic reconstructions. Both thermal and alternating field demagnetizations were carried out to isolate the characteristic remanent magnetization (ChRM). Despite the positive reversals test, rock magnetic information points to a remagnetized ChRM. The ChRM is residing in stable single-domain (SSD) magnetite grains with cogenetic superparamagnetic (SP) particles. The co-occurreance of SSD and SP magnetites generates distinct rock-magnetic properties often refer to as the 'remagnetized fingerprint' in limestones. This remagnetization process is also manifested by the widespread occurrence of gypsum veinlets in the limestones. The site-mean direction of the 12 sites after tilt-correction is $D_s = 30.6°$, $I_s = 35.6°$, $\kappa_s = 182.9$, $\alpha_{95} = 3.2°$, corresponding to a palaeolatitude of ~19.7°± 2.8°N for the study area. The corresponding palaeopole (59.8°N, 202.7°E with $A_{95} = 2.8°$) points to an NRM acquired after the India–Eurasia collision. The original sediments were likely anoxic because of the high organic carbon fluxes that prevailed during their deposition. After the India–Eurasia collision, it is envisaged that conditions became more oxic, giving rise to oxidation of iron sulphides to authigenic magnetite and the CRM acquisition. The Zaduo area in the Eastern Qiangtang Terrane has experienced ~15.7° ± 3.2° (~1740 ± 350 km) of latitudinal crustal shortening since the Eocene. In addition, the clockwise rotation responding to the India–Eurasia collision is also detected in the Zaduo area.

Key words: Magnetic properties; Asia; Palaeomagnetism; Remagnetization; Rock and mineral magnetism.

1. INTRODUCTION

The Tibetan Plateau is composed of multiple accreted terranes, including (from south to north) the Tethyan Himalaya, the Lhasa, the Qiangtang, the Songpan-Ganzi and the Qaidam-Qilian terranes. (Fig. 1). These terranes originated from the supercontinent of Gondwana, successively drifted northward and accreted to Eurasia from the Early Palaeozoic to the Late Mesozoic (Dewey *et al*. 1988; Yin

© The Author(s) 2021. Published by Oxford University Press on behalf of The Royal Astronomical Society. All rights reserved. For permissions, please e-mail: journals.permissions@oup.com

Downloaded from https://academic.oup.com/gji/article/228/3/2073/6381694 by Vakgroep Wiskunde /University Library Utrecht user on 05 January 2022

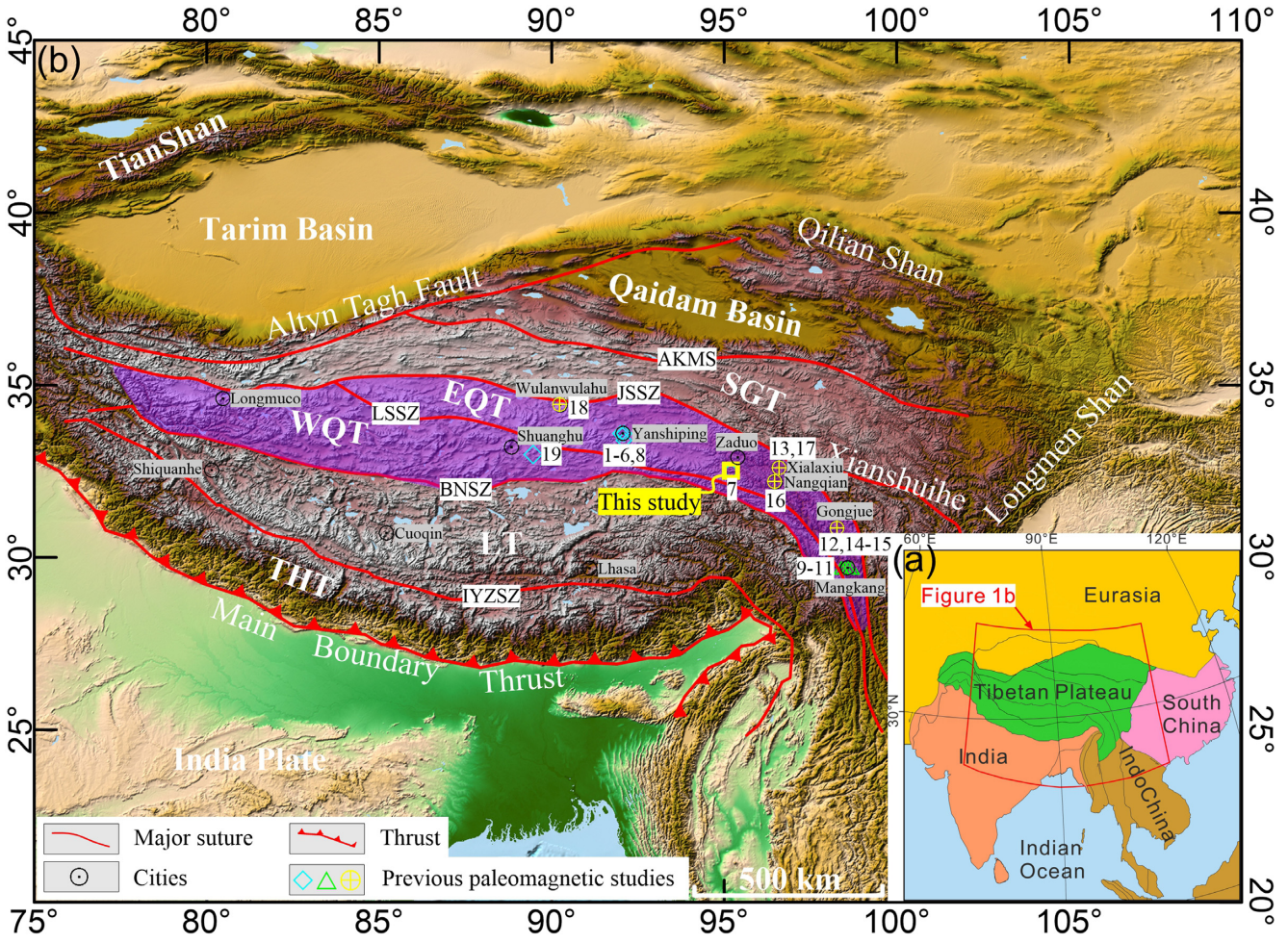

Figure 1. (a and b) Simplified tectonic map of the Tibetan Plateau and its adjacent regions (a) modified after van Hinsbergen *et al.* (2012). The abbreviations of the tectonic units are SGT: Songpan-Ganzi Terrane; EQT: Eastern Qiangtang Terrane; WQT: Western Qiangtang Terrane; LT: Lhasa Terrane; THT: Tethyan Himalaya Terrane; AKMS: Ayimaqing-Kunlun-Muztagh Suture Zone; JSSZ: Jinshajiang Suture Zone; LSSZ: Longmu Tso-Shuanghu Suture Zone; BNSZ: Bangong-Nujiang Suture Zone; IYZSZ: Indus-Yarlung Zangbo Suture Zone. The numbers show the locations of previous palaeomagnetic studies: 1 – Dong *et al.* (1991); 2 – Dong *et al.* (1990); 3 – Ran *et al.* (2017); 4 – Yan *et al.* (2016); 5 – Ren *et al.* (2013); 6 – Cheng *et al.* (2012); 7 – This study; 8 – Lin & Watts (1988); 9 – Huang *et al.* (1992); 10 – Otofuji *et al.* (1990); 11 – Tong *et al.* (2015); 12 – Li *et al.* (2020); 13 – Roperch *et al.* (2017); 14 – Tong *et al.* (2017); 15 – Zhang *et al.* (2018); 16 – Zhang *et al.* (2020a); 17 – Cogné *et al.* (1999); 18 – Lippert *et al.* (2011); 19 – Cao *et al.* (2019) (see also Table S1). The cyan, green and yellow symbols represent the previous palaeomagnetic studies of the Jurassic, Cretaceous and Palaeogene, respectively.

& Harrison 2000; Tapponnier *et al.* 2001; Kapp *et al.* 2007). Afterwards, due to the persistent northward indentation of the Indian Plate with the Eurasian Plate and the related subduction, the Tibetan Plateau was established. The Qiangtang Terrane (QT), the target terrane of this study, is a long and narrow major crustal fragment in the central Tibetan Plateau, generally thought to have separated from Gondwana in Late Palaeozoic (Yin & Harrison 2000; Metcalfe 2013; Xu *et al.* 2015). It collided with the Songpan-Ganzi Terrane (SGT) during the Late Triassic to the Early Jurassic (Roger *et al.* 2010; Song *et al.* 2015; Yan *et al.* 2016; Guan *et al.* 2021). To the south, the Lhasa Terrane accreted with the Qiangtang terrane during the Middle or Late Jurassic (Xu *et al.* 1985; Dewey *et al.* 1988; Yan *et al.* 2016; Ma *et al.* 2017; Li *et al.* 2019a, b), or the Early Cretaceous (Kapp *et al.* 2003, 2007; Zhu *et al.* 2006, 2011, 2013, 2016; Bian *et al.* 2017; Meng *et al.* 2018; Chen *et al.* 2020), even the Late Cretaceous (Zhang *et al.* 2012; Fan *et al.* 2014, 2015, 2018a, b; Liu *et al.* 2014). The different methods used to constrain the collision age are likely the foremost reason for observed differences in timing (Ding *et al.* 2005; Chen *et al.* 2020). Methods include ophiolite obduction, faunal migration, peripheral foreland basin formation and palaeomagnetism. Each delivers the age of different stages in the collision history providing sometimes an upper or a lower limit (Ding *et al.* 2017).

To quantify the drift history of the Qiangtang Terrane, many palaeomagnetic studies have been carried out on its Mesozoic strata that provided extensive knowledge on its tectonic history (Lin & Watts 1988; Dong *et al.* 1990, 1991; Otofuji *et al.* 1990; Huang *et al.* 1992; Chen *et al.* 1993, 2017; Song *et al.* 2012, 2015, 2020; Cheng *et al.* 2012; Ren *et al.* 2013; Tong *et al.* 2015; Yan *et al.* 2016; Ran *et al.* 2017; Meng *et al.* 2018; Cao *et al.* 2019, 2020; Zhou *et al.* 2019; Guan *et al.* 2021). However, despite this vast research effort, after consideration of the 'Van der Voo criteria' and the recently established 'R-criteria' (Van der Voo 1990; Meert *et al.* 2020), robust palaeomagnetic data sets are still rather limited in number given the size of the terrane. Based on palaeomagnetic studies from the same Middle-Upper Jurassic marine sedimentary rock unit (the Yanshiping Group), Cheng *et al.* (2012), Ren *et al.* (2013) and Yan *et al.* (2016) obtain palaeolatitudes of 20–25°N for

Downloaded from https://academic.oup.com/gji/article/228/3/2073/6381694 by Vakgroep Wiskunde /University Library Utrecht user on 05 January 2022

the Yanshiping area (Fig. 1), while Ran *et al*. (2017) suggest a syn-folding remagnetization acquired during the early stage of folding (about 20 per cent). In the Shuanghu area (∼300 km west of the Yanshiping area), Cao *et al*. (2019) report a Jurassic palaeolatitude of ∼35°N for their reference site. Because of this palaeolatitudinal discrepancy for the same Yanshiping Group, we investigate here the Middle-Upper Jurassic limestones of that group in the Zaduo area (∼300 km east of the Yanshiping area), in the Eastern Qiangtang Terrane.

A major challenge in palaeomagnetism studies is that remagnetization can interfere with palaeogeographic reconstructions, as is increasingly recognized (Van der Voo & Torsvik 2012). It occurs unpredictably either pre-folding (e.g. Perroud & Van der Voo 1984; Huang *et al*. 2015; Gao *et al*. 2018), syn-folding (e.g. Kent & Opdyke 1985; Ran *et al*. 2017; Huang *et al*. 2017a, b) or post-folding (e.g. Liebke *et al*. 2013; Huang & Opdyke 2015) rather than being restricted to a certain period in certain regions. Carbonate rocks are particularly notorious for being prone to remagnetization (Jackson & Swanson-Hysell 2012). For instance, widespread remagnetization has been reported in the orogenic belts in America and Europe (Zegers *et al*. 2003; Zwing *et al*. 2009; Elmore *et al*. 2012; Jackson & Swanson-Hysell 2012; Van der Voo & Torsvik 2012). Certain studies reveal carbonate remagnetization in the South China Block (Liu *et al*. 2013; Huang & Opdyke 2015; Zhang *et al*. 2020b) and the Tibetan Plateau (Appel *et al*. 2012; Liebke *et al*. 2013; Huang *et al*. 2015, 2017a, b, 2019a; Ran *et al*. 2017; Li *et al*. 2017b). It is clear that improper conclusions will be reached when using remagnetized rocks for classic palaeogeographic reconstruction.

In this paper, we present a palaeomagnetic study on Middle-Upper Jurassic limestones from the Zaduo region. Their characteristic remanent magnetization was isolated using both thermal and alternating field (AF) demagnetization. Field tests and inclination shallowing correction were carried out. Specifically, we use detailed rock magnetism experiments and microscope observation to determine whether or not the rocks had suffered remagnetization. After confirming the remagnetization, we analyse its timing along with its geological implications. Finally, we discuss possible acquisition mechanisms of remagnetization that may have been operating in this particular setting.

2. GEOLOGICAL SETTING AND SAMPLING

The Qiangtang Terrane is located in the central Tibetan Plateau, bounded by the Bangong-Nujiang Suture Zone (BNSZ) to the south with the Lhasa Terrane and by the Jinshajiang Suture Zone (JSSZ) to the north with the Songpan-Ganzi Terrane (Fig. 1b). The Triassic Longmo Co-Shuanghu suture zone (LSSZ) subdivides the terrane into the Eastern and Western Qiangtang subterranes (EQT and WQT, respectively), also known as the Northern and Southern Qiangtang subterranes (*cf*. Fig. 1b; ; Yin & Harrison 2000; Pan *et al*. 2004; QGSI 2005; Li *et al*. 2009; Metcalfe 2013).

Our sampled section (32.5°N, 95.2°E) is located in the eastern portion of the EQT, about 30 km to the south of the Zaduo County (Fig. 1b). In the Zaduo area rocks from Palaeozoic to Cenozoic age are exposed, they are separated by several unconformities, from old to young: the Lower Carboniferous Zaduo Group, the Upper Carboniferous Jiamainong Group, the Permian Kaixinling Group and Gadikao Formation, the Middle Triassic Jielong Formation, the Upper Triassic Jieza Group, the Middle-Lower Jurassic Yanshiping Group, the Cretaceous Fenghuoshan Group, the Palaeocene Tuotuohe and Luolika Groups and the Eocene Wudaoliang Quguo Groups (Fig. 2a; QGSI 2005, 2014; Guan *et al*. 2021). There is an obvious sedimentary hiatus during the Early Cretaceous (QGSI 2005, 2014). The Jurassic Yanshiping Group is formally defined in the Yanshiping area and consists of the Quemo Co (J_2q), Buqu (J_2b), Xiali ($J_{2\text{-}3}$x), Suowa (J_3s) and Xueshan (J_3x) Formations from base to top (QGSI 2005, 2014; Fang *et al*. 2016; Yan *et al*. 2016). The Group is characterized by rhythmic alternations of sandstone and limestone sequences with an overall coarsening upward pattern (QGSI 2005, 2014; Fang *et al*. 2016; Yan *et al*. 2016). All formation contacts are conformable. However, only the Quemo Co, Buqu and Xiali Formations are exposed in the Zaduo area, our study target (Figs 2a and c; QGSI 2005, 2014; Fang *et al*. 2016; Song *et al*. 2016; Yan *et al*. 2016). The Quemo Co Formation consists of alternating purple-red sandstones to mudstones with a conglomerate layer at the bottom. The Buqu Formation is mainly white-greyish to dark-greyish oolitic and bioclastic limestone deposited in shallow littoral sea. The appearance of massive biolimestones indicates a warm climate at that time, which was conducive to the growth of organisms, while its bioclastic nature reflects the shallow sea depositional conditions (QGSI 2005, 2014). Many bivalve fossils are identified in the Buqu Formation in the study area, including *Camptonectes* (*Camptochlamys*), *yanshipingensis* Wen, *Camptonectes* (*Camptonectes*) *rugosus* Wen, *Camptonectes* (*Camptonectes*) *cf*. *lens* (Sowerby), *Camptonectes concentrica* (Sowerby) and *Pholadomya socialis qinghaiensis* Wen, index fossils of the Bajocian and Bathonian Stages of the Jurassic Epoch (QGSI 2005, 2014), which are similar to those observed in the Yanshiping region that were magnetostratigraphically dated to be 165.5–163.3 Ma (Fang *et al*. 2016). The Xiali Formation consists of purple-red and yellow-green sandstones, siltstones and multicoloured (dark red, grey, greyish and light yellow) mudstones (QGSI 2005, 2014; Fang *et al*. 2016).

A total of 133 samples from 12 sites were collected from the Buqu Formation using a portable water-cooled petrol-powered drill. They were oriented with a magnetic compass and a sun compass when the weather allowed. All of the sites are located along a monoclinal section where bedding attitudes only have a slight variation with a NE dip direction and dips of 23–31° (Figs 2b, d and e). Remarkably, veins are widespread in the Buqu Formation limestones. Most of the samples were collected from fresh rock away from cracks and veins.

3. PETROGRAPHY

Veins are very common in the Buqu Formation limestones (Figs 3a–c). To better understand their mineral composition, texture and potential changes during burial, we microscopically analysed thin sections of 10 representative samples. Although we collected fresh samples away from cracks and veins, small gypsum veins can be observed on the samples (Figs 3d–h). Two different microtextures are present in these samples (Figs 3i–p). The first type is characterized by a bioclastic structure, with micritic and/or sparry calcite as the dominant groundmass. Bioclastics account for 60 per cent of the detrital component and interstitial material for the remaining 40 per cent. Extensive cementation, dissolution, replacement and recrystallization features are recognized. The bioclastics (e.g. crinoids, algae, crustaceans and foraminifera) are almost completely altered by calcite. The dissolution pores are filled and cemented with calcite (Figs 3i–l). The rocks were thus not immune to diagenetic features. The other type is mainly micritic and/or has a microcrystalline structure. Calcite is the dominant mineral with a content of about 95 per cent; bioclastics, terrigenous clastic quartz and certain opaque

Downloaded from https://academic.oup.com/gji/article/228/3/2073/6381694 by Vakgroep Wiskunde /University Library Utrecht user on 05 January 2022

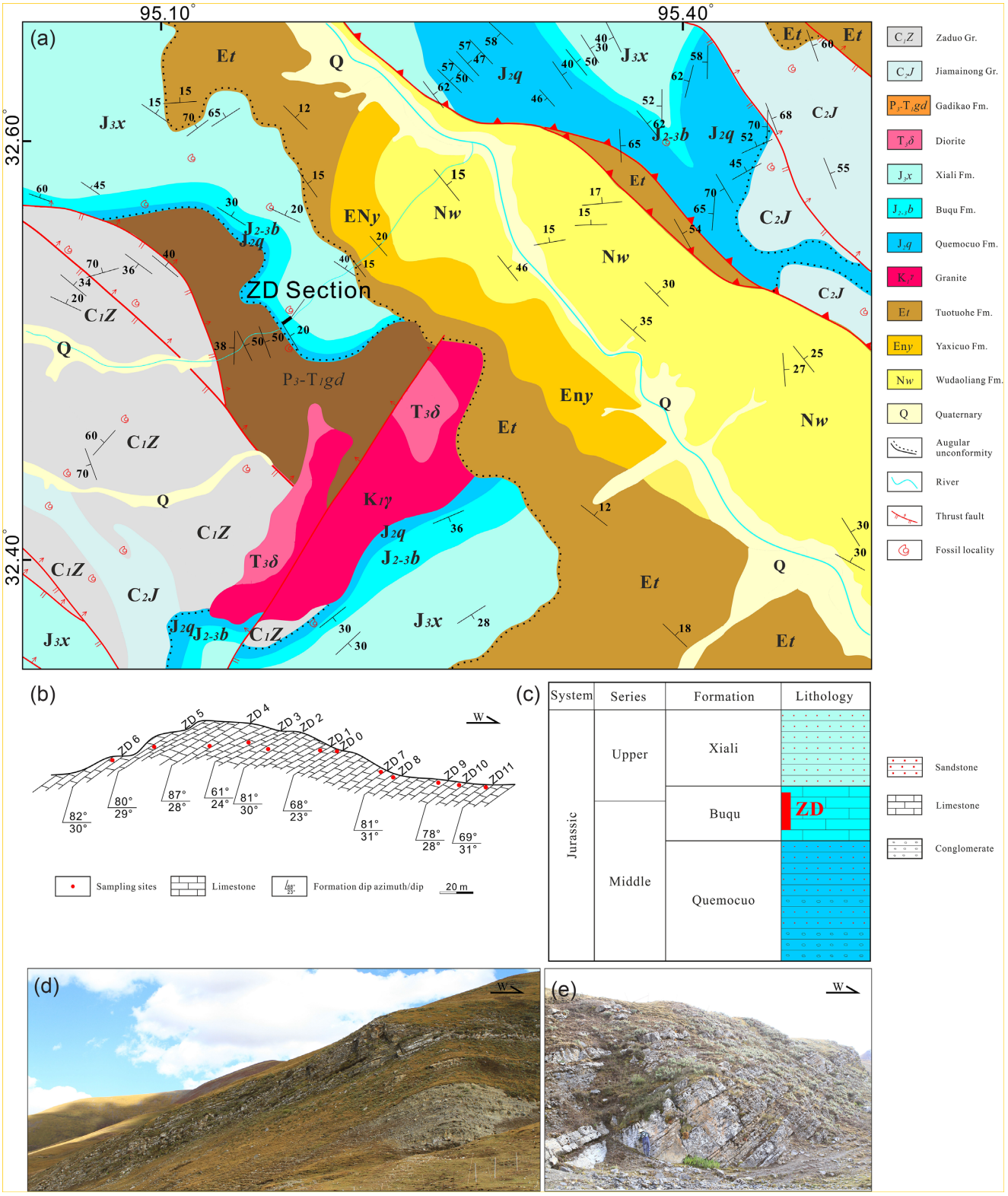

Figure 2. (a) Geological map of the Zaduo section (modified from the 1:250 000 Zaduo County regional geological map [I46C004004] by the Qinghai Geological Survey Institute (QGSI) 2005). (b) Profile of the sampled section. (c) Lithostratigraphy of the Buqu Formation with the sampling localities indicated. (d and e) Field photographs of the Buqu Formation.

Downloaded from https://academic.oup.com/gji/article/228/3/2073/6381694 by Vakgroep Wiskunde /University Library Utrecht user on 05 January 2022

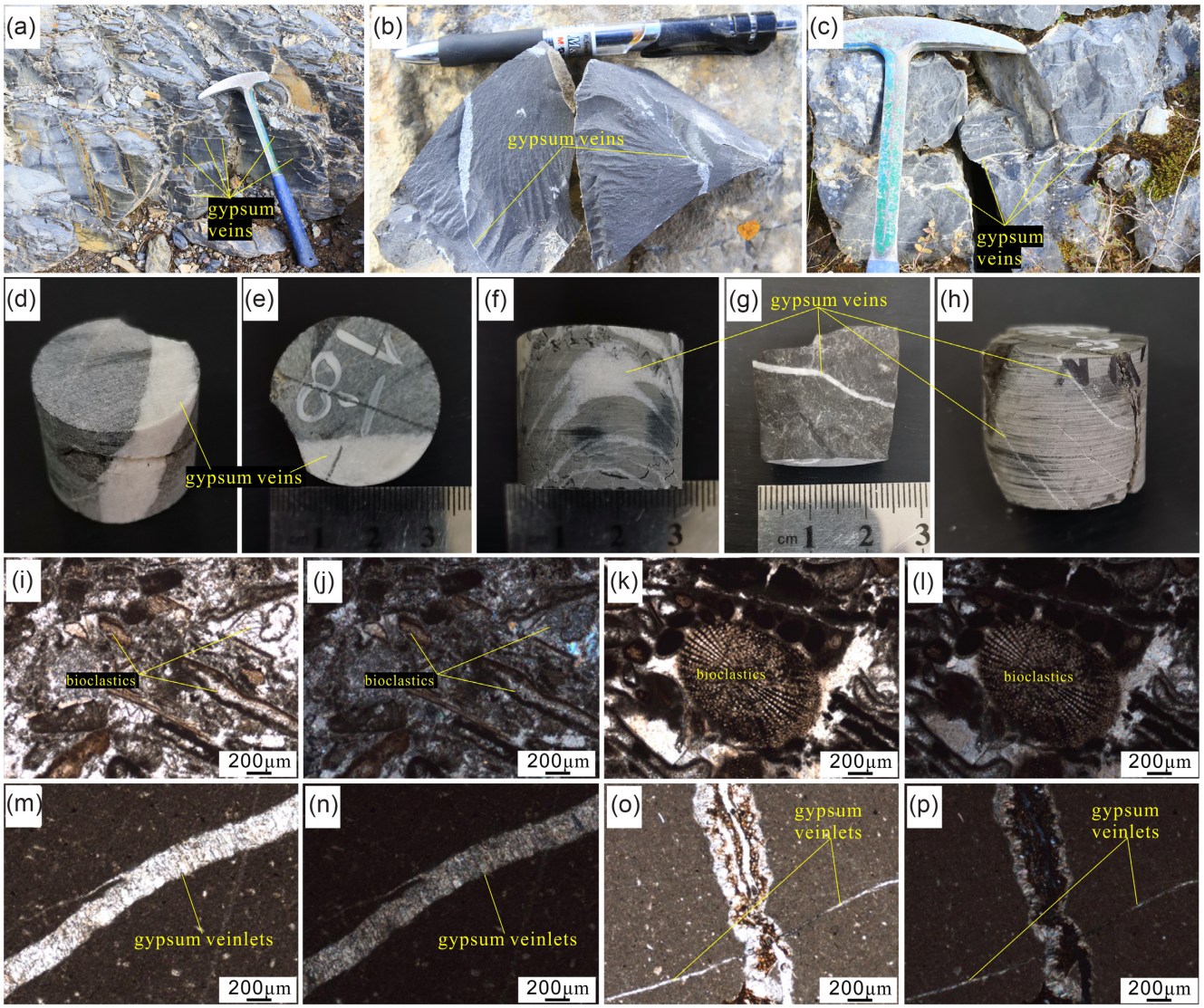

Figure 3. Results of petrographic analysis of representative samples from the Buqu Formation limestones. (a–c) Widespread veins in the field outcrops; (d–h) macroscopic gypsum veins on the surface of the samples and (i–j, k–l, m–n and o–p) micrographs in plane-polarized light and cross-polarized light.

minerals account for the remaining 5 per cent. In addition, gypsum veinlets are visible under the microscope in most of the samples investigated (Figs 3m–p). These veinlets vary in size, with a thickness ranging from a few to hundreds of micrometers. In short, the microscopic observations show widespread recrystallization and the epigenetic formation of gypsum veinlets. These features suggest hydrothermal activity with the likelihood of remagnetization (Parnell *et al*. 2000; Elmore *et al*. 2012; Ran *et al*. 2017; Huang *et al*. 2017a).

4. PALAEOMAGNETISM

Two specimens (diameter 2.5 cm, length 2.2 cm) were obtained from most of the palaeomagnetic oriented core samples, one for stepwise AF demagnetization and the other for stepwise thermal demagnetization to isolate the ChRM. Remanent magnetization measurements were conducted by a superconducting quantum interference device (SQUID) magnetometer (2G Enterprises) hosted in a magnetically shielded room (<170 nT). The AF demagnetization was conducted for 133 specimens up to an AF of 140 mT with intervals of 2–20 mT by a 2G degausser attached to the SQUID magnetometer. 25 sister specimens were progressively thermally demagnetized in 15 steps (100 °C, 150 °C, 200 °C, 300 °C, 350 °C, 400 °C, 425 °C, 450 °C, 475 °C, 500 °C, 525 °C, 550 °C, 570 °C, 580 °C and 590°C) in an ASC TD-48 oven. All of the experiments above were conducted in the palaeomagnetic laboratory of the Institute of Tibetan Plateau Research, Chinese Academy of Sciences (ITPCAS, Beijing, China).

4.1. Demagnetization

For the Buqu Formation limestones, AF and thermal demagnetization data of sister specimens show similar ChRM directions (Figs 4a–d). The ChRM directions were determined from at least four successive steps by principal component analysis (Kirschvink 1980). Specimens with maximum angular deviation (MAD) >15° were rejected for further analysis. Site-mean directions were calculated using Fisher's statistics (Fisher 1953). Given that the thermal demagnetization results were sometimes more erratic and yielded higher MAD values than the AF demagnetization, we used the latter to calculate the ChRM directions. Most of the specimens (from 10 of 12 sites) exhibit a single component that is

Downloaded from https://academic.oup.com/gji/article/228/3/2073/6381694 by Vakgroep Wiskunde /University Library Utrecht user on 05 January 2022

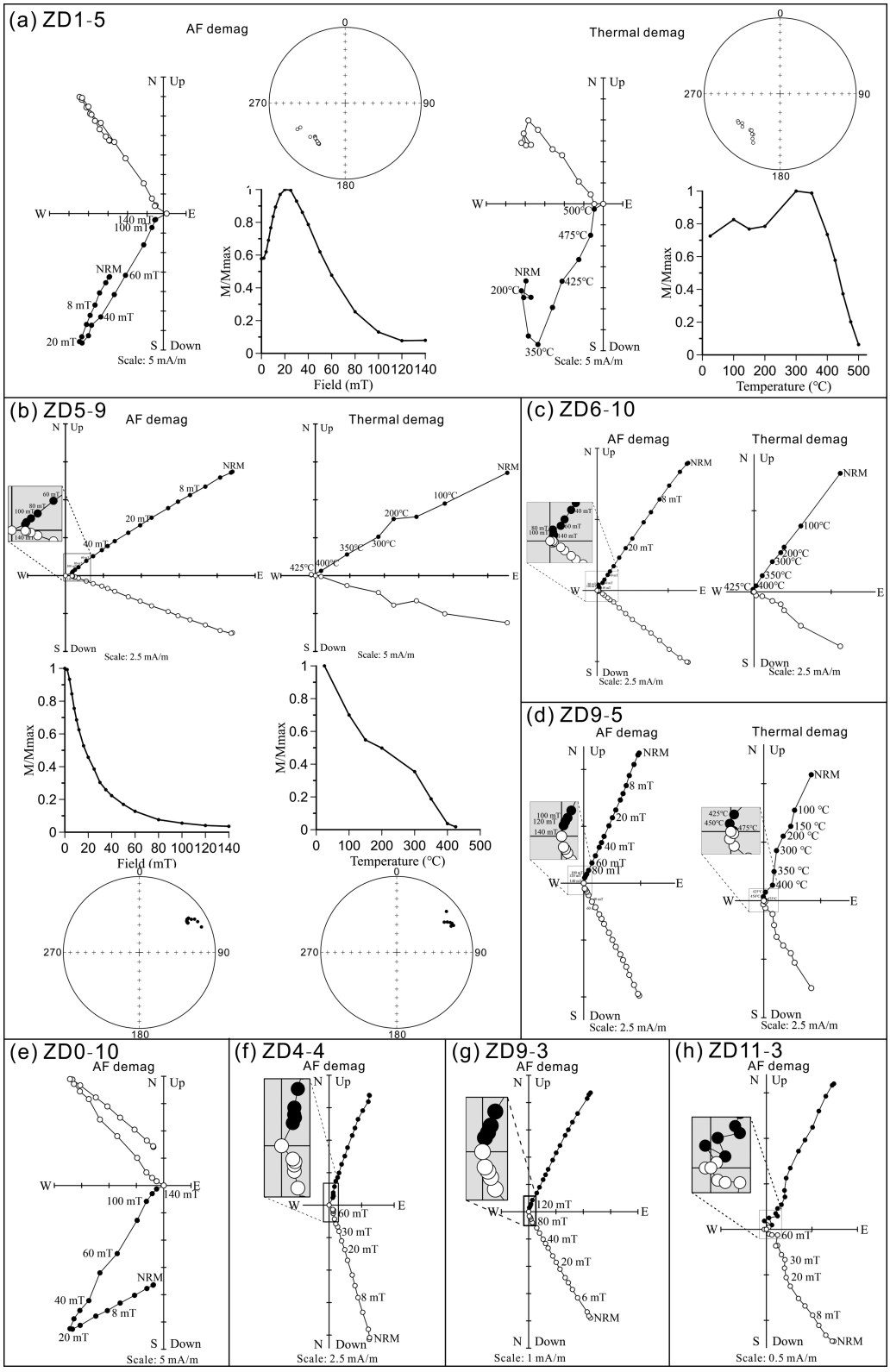

Figure 4. Representative demagnetization diagrams for specimens from the Buqu Formation limestones. All diagrams are displayed after bedding tilt correction. Solid (open) symbols represent the projections of vector endpoints on the horizontal (vertical) plane; In stereo plots, solid (open) symbols represent positive (negative) inclination. NRM: natural remanent magnetization.

Downloaded from https://academic.oup.com/gji/article/228/3/2073/6381694 by Vakgroep Wiskunde /University Library Utrecht user on 05 January 2022

decaying toward the origin (Figs 4b–d, f–h). This component was often isolated below ∼140 mT or ∼450–500 °C. The specimens' magnetic intensity usually drops to 20 per cent of the starting value below 40 mT or 350 °C (Fig. 4). The other specimens show two components (Figs 4a and e): a viscous low-field (temperature) component (LFC) which is removed below 20 mT or 300–350 °C and a high-field (temperature) component (HFC) which is isolated between 25 and 140 mT or ∼300–500 °C. These specimens have a reverse ChRM, and their magnetic intensity increased as the AF increased to 20 mT or the temperature rose to ∼350 °C (Fig. 4).

4.2. ChRM directions

The mean direction of the LFCs is $D_g = 16.4°$, $I_g = 45.0°$, $\kappa = 19$ and $\alpha_{95} = 7.1°$, $n = 22$ in geographic coordinates and $D_s = 29.1°$, $I_s = 28.1°$, $\kappa = 17.9$ and $\alpha_{95} = 7.4°$, $n = 22$ in stratigraphic coordinates (Fig. 5a). The LFCs are not clustered around the present-day geomagnetic field (PGF) direction ($D = 359.5°$, $I = 51.1°$) in this region. This component is not assigned geological significance, we thus will not speculate on its origin.

Only a single specimen from each core was palaeomagnetically processed and therefore named a sample (Butler R.F. 1992). A total of 123 of 133 specimens/samples yield consistent high AF ChRM directions that provide 12 site-mean directions containing ten normal and two reverse polarity sites (Fig. 5b and Table 1). Although the two reverse sites are grouped together stratigraphically and may not be sufficient in number, reversals test results (McFadden & McElhinny 1990) are positive at the 95 per cent confidence limit with a classification A (average $\gamma = 2.2 <$ critical $\gamma = 3.7$) for sample-mean directions and a classification B (average $\gamma = 3.6 <$ critical $\gamma = 9.0$) for site-mean directions. A fold test could not be conducted due to too slight variation of the bedding attitudes. Inclination shallowing is common in the ChRM directions derived from sedimentary rocks, and it is thought to be due to depositional processes and/or compaction during burial (Tan *et al*. 2003; Tauxe & Kent 2004; Yan *et al*. 2005; Ren *et al*. 2013). However, unlike redbeds and other clastic rocks, it is commonly believed that limestone has little inclination shallowing, as it barely compacts, typically 10 times less than redbeds (Cheng *et al*. 2012). To check whether there is indeed no inclination shallowing in the present sample collection, we applied the E/I method of Tauxe & Kent (2004) on the obtained 123 directions. The corresponding flattening factor ($f = 0.936$) provides a mean inclination of 37.4° (Figs 5d and e) with 95 per cent confidence limit bounds of 35–44°, which is a little larger than both of the sample-mean inclination (36.3°) and the site-mean inclination (35.6°), but still well within the confidence limit. Therefore no inclination bias is present in the Buqu Formation limestones in the Zaduo area. The site-mean direction of the 12 sites is $D_g = 8.2°$, $I_g = 48.3°$, $\kappa_g = 138.3$, $\alpha_{95} = 3.7°$ in situ, and $D_s = 30.6°$, $I_s = 35.6°$, $\kappa_s = 182.9$, $\alpha_{95} = 3.2°$ after tilt-correction, corresponding to a palaeopole at 59.8°N, 202.7°E with $A_{95} = 2.8°$ and a palaeolatitude of ∼19.7° ± 2.8°N for the study area (Fig. 5c and Table 1).

5. ROCK MAGNETISM

At least one representative sample from each site was selected for rock magnetic experiments. The low-field magnetic susceptibility as function of temperature (κ–T) was measured with a MFK1-FA Kappabridge instrument with a CS-4 high-temperature furnace (AGICO, Czech Republic) in an argon atmosphere at a flow rate of 100 ml min^{-1}. The successive peak temperatures were 250, 350, 400 (partially), 450, 550, 620 and 700 °C, respectively. These samples were first heated to 250 °C and cooled back to room temperature with an applied magnetic field of 200 A/m at a frequency of 976 Hz, then heated to 350 °C and cooled back to room temperature. The procedure was completed after repeating this cycle to 700 °C. Isothermal remanent magnetization (IRM) acquisition curves, direct current back field remagnetization curves, hysteresis loops, and first-order reversal curves (FORCs) were measured with a Lakeshore 8600 Vibrating Sample Magnetometer (VSM). Stepwise thermal demagnetization of IRM was conducted with a TD-48 oven and a minispin magnetometer.

5.1. Thermomagnetic runs of magnetic susceptibility

Stepwise thermomagnetic runs of magnetic susceptibility were carried out for the Buqu Formation limestones (Fig. 6). The samples show a prominent increase in magnetic susceptibility at ∼330 or 350 °C except site ZD 2 (Figs 6a, c and d), which can be attributed to magnetite formed as high temperature product of iron sulfide alteration (i.e. pyrite, pyrrhotite and greigite, Huang *et al*. 2019a). All of the 250 °C and some of the 350 °C heating-cooling cycles are reversible. The cooling curve is above the heating curve for all the 450 °C cycles. When it comes to the higher temperature interval (i.e. the 620 and 700 °C runs), some of the heating-cooling cycles are quasi-reversible. All of the samples show a decrease in susceptibility at ∼580 °C, which is typical for magnetite. A distinct increase at ∼400–500 °C of high temperature interval is likely the Hopkinson peak, suggesting fine grain size magnetite with a rather narrow grain size range as expected for magnetite formed during the experiment itself (Figs 6c and d).

5.2. IRM acquisition and back-field curves, thermal demagnetization of IRM and IRM component analysis

The IRM acquisition curves of the representative samples show similar characteristics (Figs 7a, c and d). They present a sharp increase below 100 mT and acquire ∼80–90 per cent saturation at that step, with the remanent acquisition coercive force <50 mT, suggesting that low-coercivity magnetic components (i.e. magnetite sensu lato) are dominant. Samples from site ZD 2 (Fig. 7b, note the unit of the vertical axis) are very noisy because of their weak IRM. In addition, two perpendicular IRMs with fields of 2.5 T and 120 mT were imparted in a single sample and subjected to stepwise thermal demagnetization along the lines of Lowrie (1990). The soft and hard components in most of the samples exhibit a maximum unblocking temperature at ∼500 °C (Figs 7e, g and h). This is too low for the typical SD magnetite, but compatible with the fine-grained quasi-superparamagnetic magnetite. For the samples from site ZD 2, the soft component exhibits the same features as in the others, but the hard component drops to essentially zero at ∼640 °C, which is interpreted to indicate probably fine-grained hematite as a carrier (Fig. 7f).

To estimate the magnetic contributions of different magnetic minerals, we applied IRM component analysis to a sample of each site except the reverse polarity sites (Kruiver *et al*. 2001). Four IRM components are used to fit the IRM acquisition curves: component 1 with $B_{1/2}$ [the field at which half of saturation isothermal remanent magnetization (SIRM) is reached] of ∼5 mT and dispersion parameter DP (width of the distribution) of ∼0.20–0.30 (log units); component 2 with $B_{1/2}$ of ∼10–20 mT and DP of ∼0.20–0.30; a

Downloaded from https://academic.oup.com/gji/article/228/3/2073/6381694 by Vakgroep Wiskunde /University Library Utrecht user on 05 January 2022

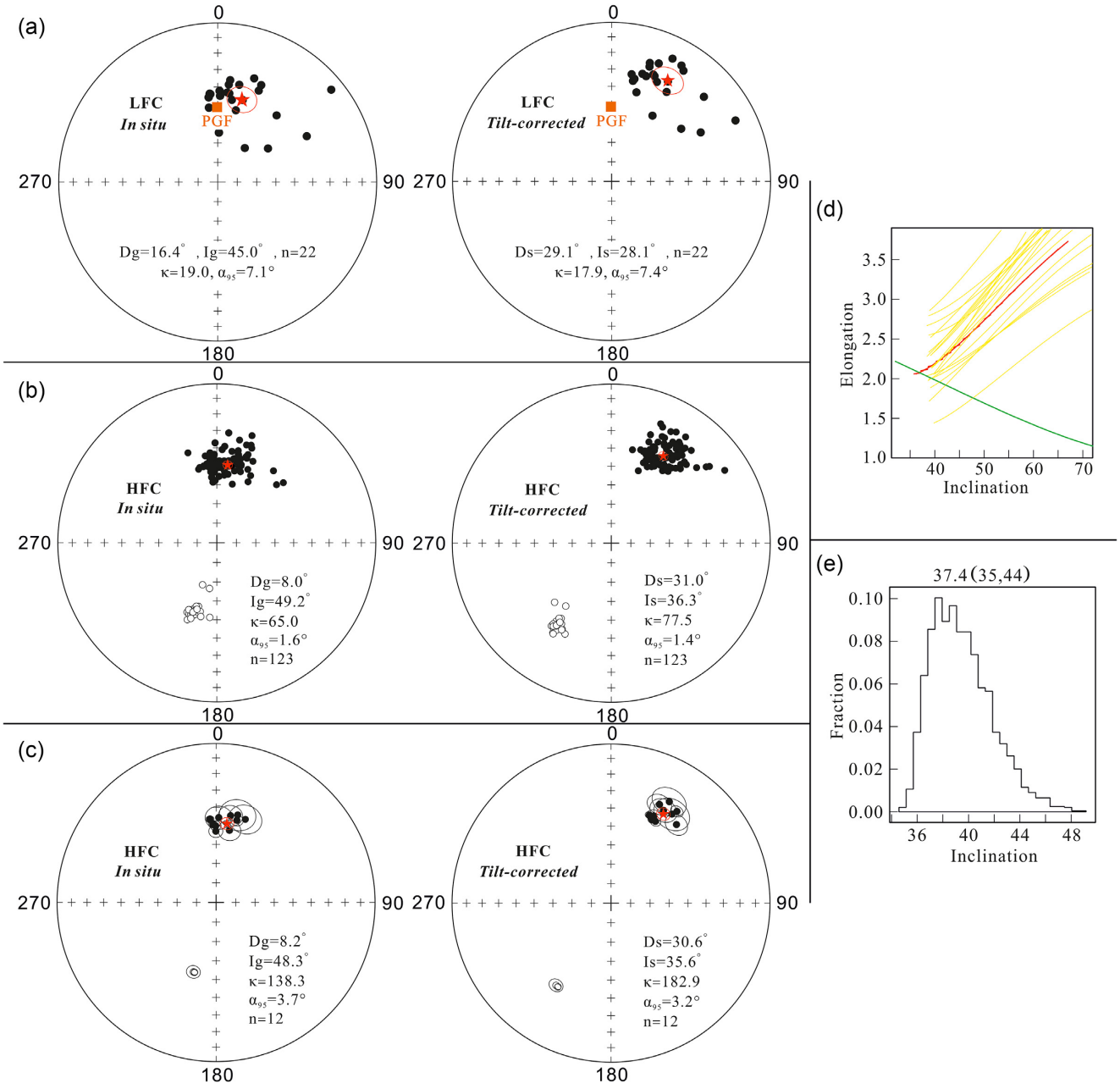

Figure 5. (a and b) Equal-area projections of the sample-mean directions for LFCs/HFCs before and after tilt correction, respectively; (c) equal-area projections of the site-mean directions for HFCs before and after tilt correction; (d) plot of elongation versus inclination derived from the TK03. GAD model, the intersection point indicates the inclination/elongation pairs most consistent with the TK03.GAD model and (e) histogram of 1000 boot-straps, the most frequent inclination is 37.4°, and the 95 per cent confidence limits are 35–44°. Red stars and circles around them in panels (a), (b) and (c) denote the overall mean direction and the 95 per cent confidence limit. The brown squares in panels (a) and (b) denote the present-day geomagnetic field (PGF) direction of the sampling location. Solid and open symbols denote the lower and upper hemispheres projections before and after tilt correction, respectively.

harder component 3 with $B_{1/2}$ of ∼50–70 mT and DP of ∼0.30; and a much harder component 4 with $B_{1/2}$ of > 300 mT and DP of <∼0.20. In general, components 1 and 2 contribute ∼10–20 per cent to the SIRM and might be the result of thermally activated component 3 (Egli 2004; Heslop *et al*. 2004; Huang *et al*. 2015; Zhang *et al*. 2018). Component 3 is the dominant magnetic carrier in the Buqu Formation limestone and contributes >70 per cent to the SIRM, which is typically interpreted to be magnetite (Kruiver *et al*. 2001). Component 4 has a distinctly $B_{1/2}$ value and contributes ∼4 per cent to the SIRM, which presumably represents very fine-grained magnetite close to the SP threshold size, or residual iron sulfide that remained after oxidation to authigenic magnetite.

5.3. Hysteresis loops, day-plot and FORC diagrams

Hysteresis loops of the Buqu Formation limestone samples can be divided into two types. Type one is from sampling site ZD 2 and shows 'pot-bellied' features (Fig. 8b). Type two samples are all from

Downloaded from https://academic.oup.com/gji/article/228/3/2073/6381694 by Vakgroep Wiskunde /University Library Utrecht user on 05 January 2022

Table 1. High-field component (HFC) directions of the Middle Jurassic limestones in the Zaduo area, Eastern Qiangtang Terrane, Tibetan Plateau.

Sites	*n*/*N*	D_g (°)	I_g (°)	D_s (°)	I_s (°)	κ_{95}	α_{95} (°)
Zaduo section (32.5°N, 95.2°E)							
ZD 0	11/12	198.1	− 52.1	213.8	− 37.8	177.1	3.4
ZD 1	12/12	197.2	− 52.1	212.4	− 37.7	945.8	1.5
ZD 2	10/10	9.5	43.9	26.2	31.5	72.7	5.7
ZD 3	7/10	19.4	43.8	29.9	27.3	50.6	7.9
ZD 4	8/11	13.9	42.7	34.4	32.7	42.1	8.6
ZD 5	9/9	10.5	51.9	39.8	35.9	102.3	5.5
ZD 6	12/12	14.2	45.7	35.7	29.7	211.3	3
ZD 7	10/11	1.8	45.6	29.5	33.4	57.1	6.4
ZD 8	11/11	359.7	50.1	28.5	41.1	316	2.6
ZD 9	12/12	357.6	49.2	26.1	41.1	481.3	2
ZD10	11/11	355.8	46.4	23.5	39.5	551.6	1.9
ZD11	10/12	359.8	53	26.2	38.8	208.8	3.4

Note: *n*/*N*, number of samples used to calculate mean and measured; D_g, I_g, D_s, I_s, declination and inclination in geographic and stratigraphic coordinates, respectively; κ_{95}, the best estimate of the precision parameter and α_{95}, the radius that the mean direction lies within 95 per cent confidence.

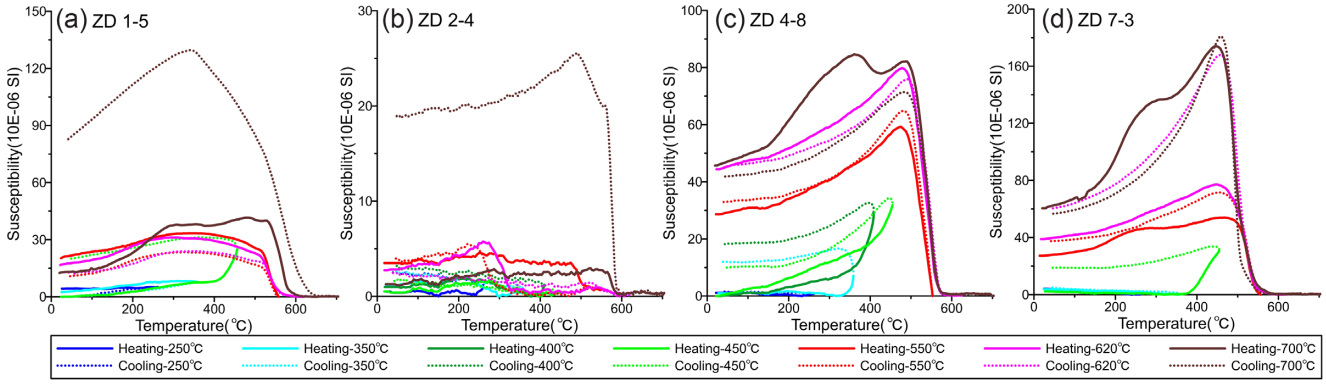

Figure 6. Multicycle high-temperature magnetic susceptibility curves (κ–T) of the representative samples.

most of the sampling sites and are characterized by 'wasp-waisted' loops (Figs 8a, c and d). 'Wasp-waisted' hysteresis loops are indicative of discrete low-coercivity and high-coercivity phases in a single sample (e.g. Roberts *et al*. 1995; Tauxe *et al*. 1996; Jackson & Swanson-Hysell 2012; Ge *et al*. 2017; Shen *et al*. 2020). This hysteresis behaviour results from multiple mineralogies or discrete fractions of ferrimagnetic grains in a largely mono-mineralic population (Jackson & Swanson-Hysell 2012). The FORC diagrams for type one samples are characterized by closed concentric contours with a substantial vertical spread of the FORC distribution, indicating an assemblage of interacting SD particles (Roberts *et al*. 2006, 2014). For type two samples (of normal polarity), FORC diagrams have a FORC density (ρ) peak (mixed second derivative of the magnetization data) with closed counters around $B_c < 20$ mT and a vertically asymmetrical distribution of about ∼−30–5 mT along the $B_c = \sim$0–5 mT line. These characteristics resemble those of SP ferrimagnetic grain assemblies (Pike *et al*. 2001; Roberts *et al*. 2006, 2014). All the samples fall within the pseudosingle domain (PSD) field on the Day plot (Dunlop 2002), with Bcr/Bc ratios ranging from 2 to 8 and M_{rs}/M_s ratios ranging from 0.1 to 0.4 (Fig. 8i). However, it should be noted that most natural sediment samples fall within the PSD domain, which makes interpretation rather complicated (e.g. Qin *et al*. 2008; Li *et al*. 2017a; Cao *et al*. 2019; Guan *et al*. 2021). Despite skepticism some people have pertaining to the Day-plot, remagnetization may be diagnosed with it (Roberts *et al*. 2018).

6. DISCUSSION

6.1. Does the Buqu Formation in the Zaduo area carry a primary NRM?

The limestones of the Buqu Formation in the Yanshiping area were dated to the Bajocian–Callovian stages based on biostratigraphic age constraints (QGSI 2005, 2014; Fang *et al*. 2016; Yan *et al*. 2016). In this study all of the samples, cq. sites, are from a monoclinal section with only a slightly varying bedding attitude. This precludes usage of the classic fold test to constrain the timing of their NRM. While the reversals test is positive which yields some support for a primary origin of the NRM, we should not exclude protracted remagnetization which may yield dual polarities (Meijers *et al*. 2011; Huang & Opdyke 2015; Huang *et al*. 2019a). In addition to the classic geometric palaeomagnetic field tests (i.e. the fold test, conglomerate test, reversals test, and baked contact test), rock magnetic characterization and microscopic observation provide valuable information to evaluate the origin and significance of NRM components.

Authigenic magnetite, dominantly in the SP and SSD size range, is rather commonly used as a 'fingerprint' of remagnetization (McCabe & Channell 1994; Jackson & Swanson-Hysell 2012). Our rock magnetic results show that magnetite is the dominant magnetic carrier in the Buqu Formation limestones. Magnetic properties differ

Downloaded from https://academic.oup.com/gji/article/228/3/2073/6381694 by Vakgroep Wiskunde /University Library Utrecht user on 05 January 2022

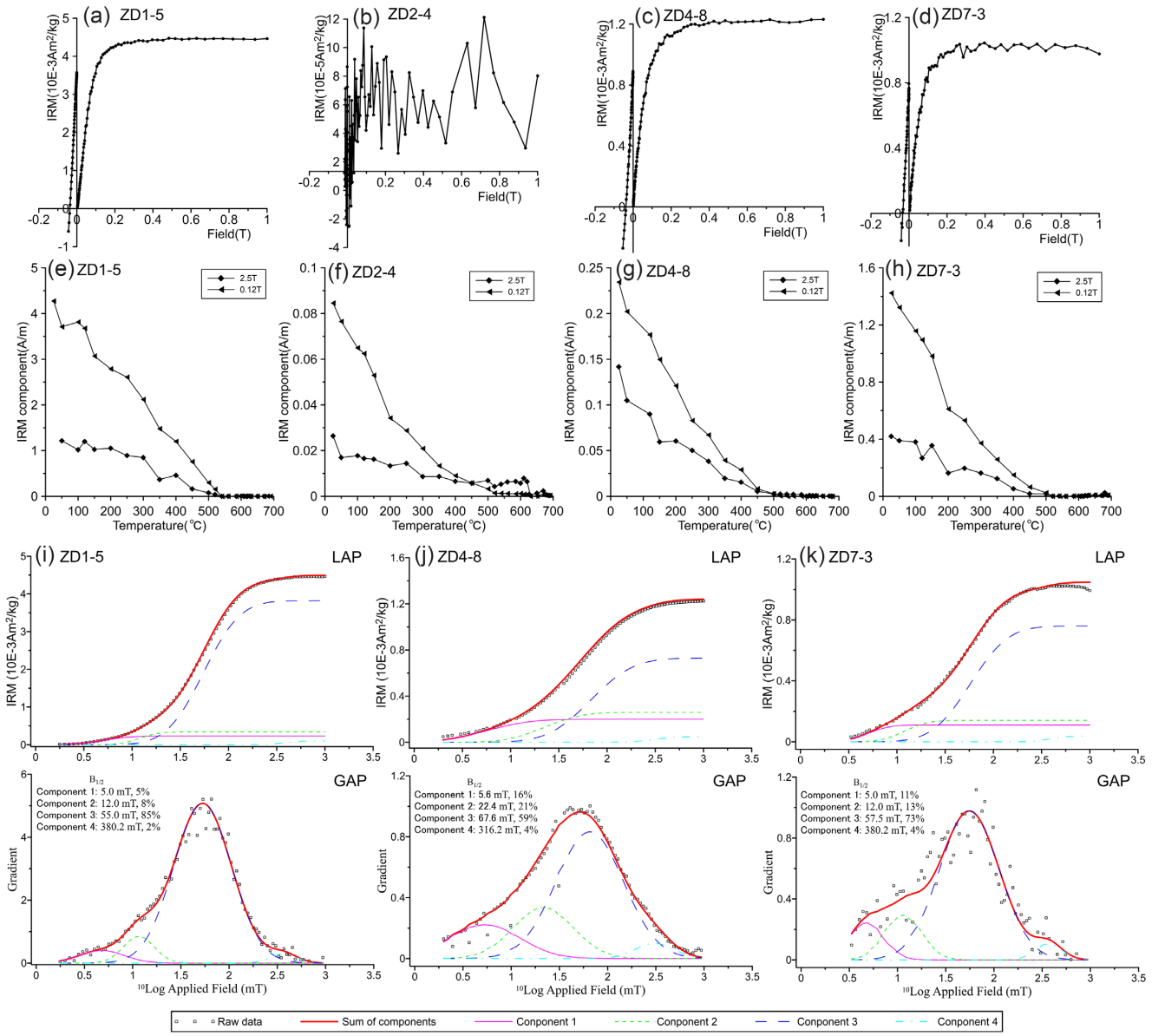

Figure 7. (a–d) IRM acquisition curves for representative samples; (e–h) Thermal demagnetization of two perpendicular IRMs; (i–k) IRM component analysis (Kruiver *et al*. 2001) of representative samples with ∼80 data points acquired. Squares are measured data points. The components are marked with different coloured lines. Log_{10} ($B_{1/2}$) and DP are in $\log_{10}$ mT. LAP: linear acquisition plot and GAP: gradient acquisition plot.

widely with increasing size within the SP range and across the SP–SSD threshold: large SP particles more often saturate in low applied fields, while small SP particles may not saturate at all even in 2 T fields (e.g. Dekkers & Pietersen 1991; Tauxe *et al*. 1996; Gong *et al*. 2009). In such cases, the 'wasp-waisted' hysteresis behaviour can be attributed to SP and SSD grain sizes of magnetite. SP particles are also indicated by the FORC features and low unblocking temperatures (400–500 °C). Although the SP particles play no role in carrying a geologically stable NRM at room temperature, they are considered to have a similar origin as the cogenetic SSD particles that do carry the palaeomagnetic information in many remagnetized carbonate rocks (e.g. Jackson & Swanson-Hysell 2012; Huang *et al*. 2019b). Coercivity (B_{cr}/B_c) and remanence (M_{rs}/M_s) ratios for our Jurassic limestones are close to the 'remagnetization trend' on a Day-plot (Fig. 8i), previously interpreted to be characteristic of chemical remagnetization (e.g. Jackson 1990; McCabe & Channel 1994; Jackson & Swanson-Hysell 2012). This trend is distinct from the regions occupied by most other rocks, sediments and synthetic materials and arguably the biggest success of the Day plot (Fig. 8i, Roberts *et al*. 2018). The uncommon magnetic properties of remagnetized carbonates display an empirically derived equation of $M_{rs}/M_s \approx 0.89(B_{cr}/B_c)^{-0.6}$ (Jackson 1990; Jackson *et al*. 1993). Our data show a trendline similar to this equation, except that the M_{rs}/M_s values of our samples are lower than those in Jackson's (1990) study, which can be attributed to partial oxidation of magnetite, particle shape, or uncertain mixtures of magnetic mineral components (Roberts *et al*. 2018). Our data will fit well if we would change the trendline equation to $M_{rs}/M_s \approx 0.89(B_{cr}/B_c)^{-1}$ or $M_{rs}/M_s \approx 0.5(B_{cr}/B_c)^{-0.6}$as proposed by Jackson *et al*. (1993); the best-fitting equation of our data is $M_{rs}/M_s \approx 0.61(B_{cr}/B_c)^{-0.8}$ (Fig. 9).

In the study area, veins are widespread in the Buqu Formation limestones. Evidently, we focused on fresh rocks away from cracks

Downloaded from https://academic.oup.com/gji/article/228/3/2073/6381694 by Vakgroep Wiskunde /University Library Utrecht user on 05 January 2022

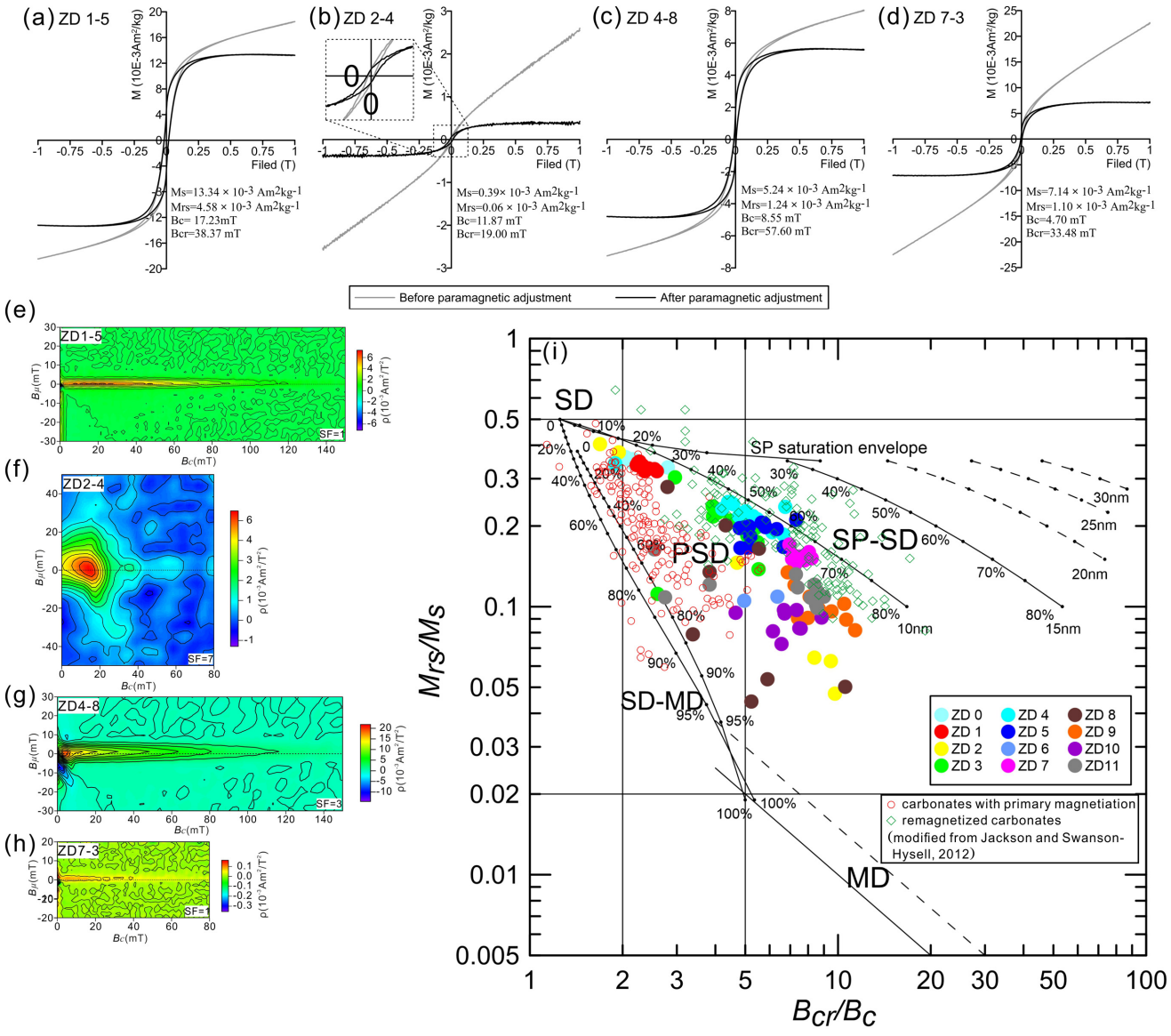

Figure 8. (a–d) Hysteresis loops of representative samples; the grey and black loops are before and after correcting for the paramagnetic contribution, respectively; (e–h) FORC diagrams for representative samples; (i) Day plot (Dunlop 2002) of 114 limestone samples. Also plotted are Day-plot of published hysteresis parameters for remagnetized and non-remagnetized carbonate rocks summarized by Jackson & Swanson-Hysell (2012). Solid dots denote different sampling sites from the ZD section, green diamonds and red circles denote remagnetized and non-remagnetized carbonate rocks from Jackson & Swanson-Hysell (2012), respectively.

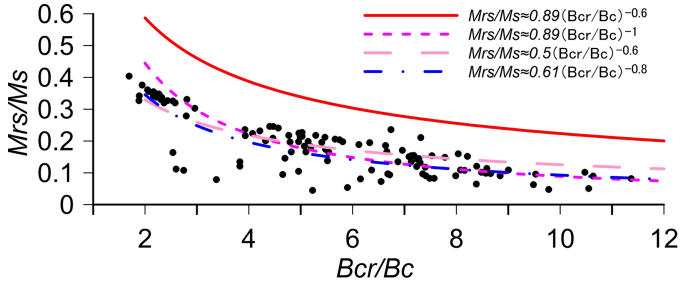

Figure 9. Hysteresis parameters for the Jurassic limestones in the Zaduo section and empirically derived equation of remagnetized carbonates. The red line represents the equation from Jackson (1990) and Jackson & Rochette (1993); the magenta short dashed and pink long dashed lines represent the modified equations Jackson & Rochette (1993); the blue dash–dotted line represents the best-fitting equation of our data.

Downloaded from https://academic.oup.com/gji/article/228/3/2073/6381694 by Vakgroep Wiskunde /University Library Utrecht user on 05 January 2022

and veins to collect samples. However, veins of a few to a dozen millimeters wide can be clearly observed on the surface of some core samples (Fig. 3). For those core samples whose veins are invisible by observation with the naked eye, a few to tens of microns wide veins can be observed under the microscope (Fig. 3). These veins are mainly composed of gypsum, commonly taken as being indicative of diagenetic fluid migration (Gustavson *et al*. 1994; Philipp 2008; Bons *et al*. 2012; Gale *et al*. 2014), so, quite reasonably associated with remagnetization of the Buqu Formation limestones in the study area. Therefore, rock magnetic tests and thin section observations lead us to conclude that the studied Jurassic limestones of the Buqu Formation in the Zaduo area were remagnetized. Authigenic magnetite grains, dominantly of SSD size, but with cogenetic fine-grained SP size particles, are responsible for the secondary magnetizations.

6.2. Timing of the remagnetization and tectonic implications

Remagnetization can occur in principle any time during geological history, yet it is generally tied to certain geological events (e.g. diagenesis, orogenies, metamorphism, or thermoviscous resetting by volcanism). Two major events have occurred in the Tibetan Plateau region after the middle Jurassic: one is the collision between the Lhasa and Qiangtang Terranes, and the other is the India–Eurasia collision. The shortest distance from a remagnetization palaeopole to the reference apparent polar wander path (APWP) can be used to estimate the age of the remagnetization event in spite of the rather low precision of this approach (Van der Voo & Torsvik 2012). Here we compare the palaeopole from the present study with those from the Eastern Qiangtang Terrane. The Jurassic to Palaeogene palaeopoles of the Eastern Qiangtang Terrane were selected for consideration following the restrictive criteria for high-quality palaeomagnetic data (Fig. 10a and Table 2). As shown in Fig. 10(a) and Table 2, the Jurassic palaeopoles (Cheng *et al*. 2012; Ren *et al*. 2013; Yan *et al*. 2016) are consistent. However, the Cretaceous and Palaeogene palaeopoles are more scattered, which is interpreted as local rotation after the Lhasa–Qiangtang and India–Eurasia collisions (Tong *et al*. 2015; Chen *et al*. 2017). Even in the presence of different coeval palaeopoles, the palaeopole of this study (59.8°N, 202.7°E, $A_{95} = 2.8°$) is fairly close to the sparsely available Palaeogene poles (see the supporting information text and Table S1; Fig. 10a; Van der Voo 1990; Meert *et al*. 2020). We also calculated the mean inclinations of the Jurassic, Cretaceous and Palaeogene, our inclination (35.6° ± 4.2°) is similar to the Jurassic (34.7° ± 5.2°) and the Palaeogene (39.7° ± 7.3°) inclinations, but smaller than the Cretaceous inclination (52.8° ± 6.1°).

Alternatively, the timing of remagnetization can be estimated by comparison of the measured declination, inclination and palaeolatitude with the expected ones for different ages in the Qiangtang Terrane. All the palaeomagnetic directions were converted to our study site (32.5°N, 95.2°E), the new declinations and palaeolatitudes were then recalculated and are shown in Figs 10(c) and (d). Palaeomagnetic declinations indicate that the Qiangtang Terrane relative to Eurasia experienced ∼20° counterclockwise rotation since the Middle-Late Jurassic, ∼30–40° clockwise rotation since the Cretaceous (Huang *et al*. 1992; Tong *et al*. 2015), and ∼10–30° clockwise rotation since the Palaeogene (Lippert *et al*. 2011; Tong *et al*. 2017; Zhang *et al*. 2018, 2020a; Li *et al*. 2020). The fold in our study area was formed during the late Himalayan period (QGSI 2014). The ChRM directions after tilt-correction ($\kappa_s = 182.9$) are more clustered than in geographic coordinates ($\kappa_g = 138.3$, Figs 5b and c). It is likely that the remagnetization occurred prior to the folding. The declination after correction for the bedding attitude in this study is ∼30°, which is comparable with either the Cretaceous or the Palaeogene declination. Notably, the Early Cretaceous intrusive rock body nearby has an age of ∼126 Ma (QGSI 2014) which is plausible to account for the remagnetization, considering that ∼126 Ma is fairly close to a N/R polarity transition (in the timescale of Gale *et al*. 2020, there is a normal-polarity zone from ∼127.6 to ∼126.5 Ma and a reversed-polarity zone from ∼126.5 to ∼124.7 Ma) which could account for the dual polarities found in this study. However, upon further analysis, this scenario seems unlikely (see section 6.3). Furthermore, dual-polarity makes it not likely that the remagnetization has occurred during the Cretaceous Normal Superchron (CNS), even though a very recent study suggests several reverse-polarity events or clusters of events within the CNS (Zhang *et al*. 2021). Inclination matching and palaeolatitude matching were used to determine the remagnetization age. The palaeolatitude of ∼31–36° N obtained from the Mangkang area is about ∼10–15° higher than that of this study (∼20°N), but with large uncertainty in their studies (±6.5° to ±10.9°, Huang *et al*. 1992; Tong *et al*. 2015). In contrast, the 38.6 ± 0.5 Ma palaeomagnetic data from the Wulanwulahu area indicate that the Eastern Qiangtang Terrane was at a palaeolatitude of ∼25°N at that time (Lippert *et al*. 2011). This is consistent with the inclination-shallowing-corrected result of ∼24°N during the interval from 56.0 to 43.2 Ma by Tong *et al*. (2017). In addition, these palaeolatitudes are similar to the predicted palaeolatitude of the Eastern Qiangtang Terrane of ∼24–30° N, a prediction based on magnetostratigraphic data of the sedimentary sequences in the Nangqian and Gongjue basins (Zhang *et al*. 2020a; Li *et al*. 2020). We therefore interpret that the episode of remagnetization studied here more likely occurred during the Eocene rather than the Cretaceous.

The collision between India and Eurasia during the Palaeocene induced significant latitudinal crustal shortening across southern Eurasia (Dewey *et al*. 1989; Yin & Harrison 2000; Dupont-Nivet *et al*. 2010a, b; Lippert *et al*. 2011; van Hinsbergen *et al*. 2012; Li *et al*. 2017c; Tong *et al*. 2017). The expected palaeolatitude of the reference point (32.5°N, 95.2°E) calculated from the Eocene reference poles for Eurasia is ∼35°N, indicating that the Zaduo area of the Eastern Qiangtang Terrane has experienced ∼15.7° ± 3.2° (∼1740 ± 350 km) of latitudinal crustal shortening since the Eocene. The large difference in latitudinal crustal shortening between the Zaduo and Mangkang areas would likely be accommodated by strike-slip faulting. However, strike-slip faulting is non-existent in the Eastern Qiangtang Terrane, either due to palaeomagnetic data uncertainty, or alternatively due to clockwise rotations of the Mangkang area that would yield southward movements of the region, which indeed have been documented by some studies (e.g. Huang *et al*. 1992; Tong *et al*. 2015). Also, a combination of both options is possible. Given that the palaeomagnetic data generally come with statistical uncertainties >4°, sometimes even >10°, in our view, it is less relevant to discuss possible north/south movements of the Qiangtang Terrane for the period involved, because the data uncertainty is not really justifying that. Our estimates coincide with latitudinal shortening estimates across Tibet and stable Eurasia in a number of palaeomagnetic studies (Dupont-Nivet *et al*. 2010a, b; Tang *et al*. 2013; Ma *et al*. 2014; Li *et al*. 2017c; Tong *et al*. 2017). In response to the India–Eurasia collision, the southeastern part of the Tibetan Plateau underwent a clockwise rotation (Tapponnier *et al*. 1982). The Zaduo area, Nangqian, Xialaxiu, Gongjue and Mangkang basins are all located in the transition zone where the

Downloaded from https://academic.oup.com/gji/article/228/3/2073/6381694 by Vakgroep Wiskunde /University Library Utrecht user on 05 January 2022

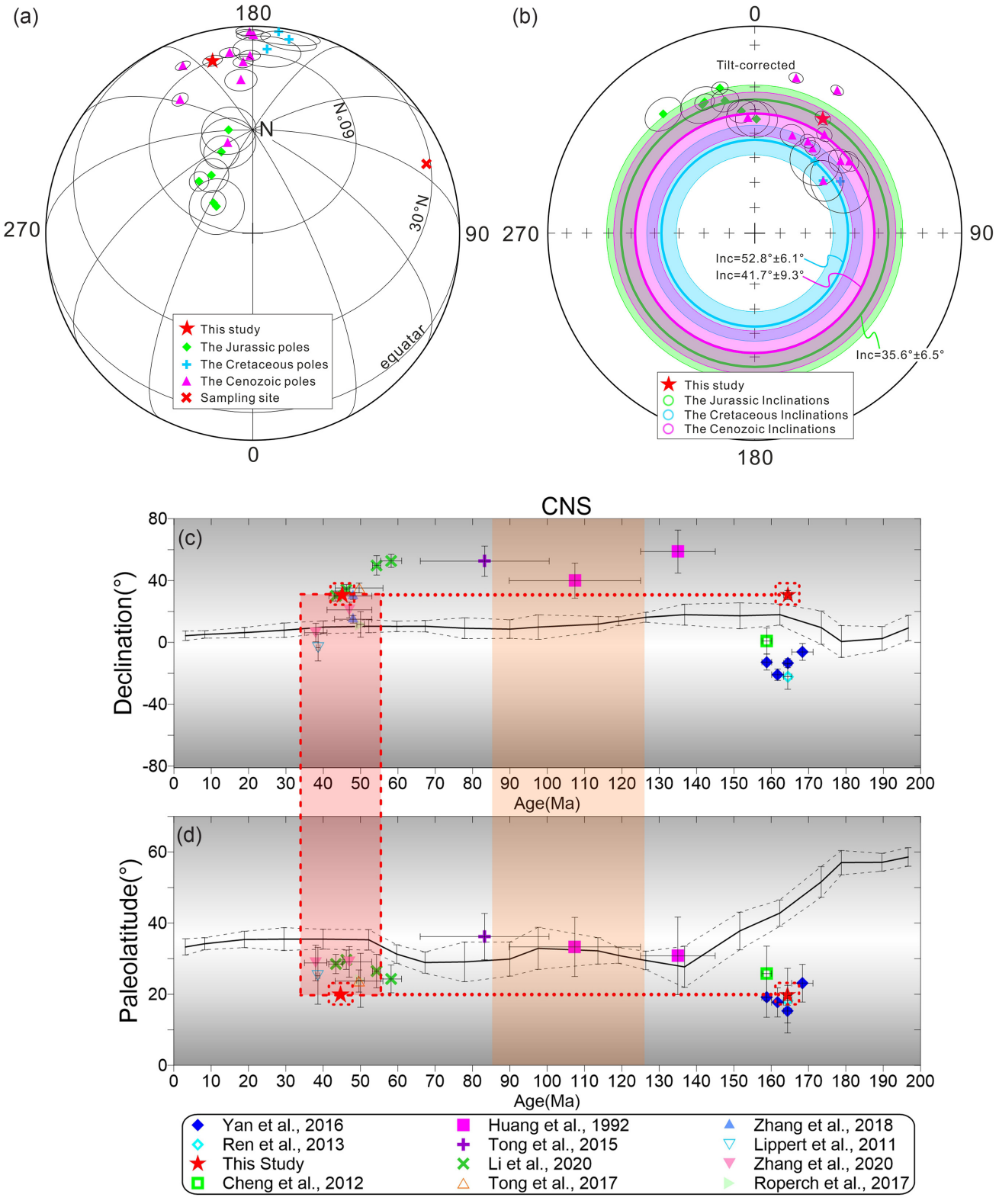

Figure 10. (a) Equal-area projection of the reliable Jurassic, Cretaceous and Cenozoic palaeopoles obtained from the Eastern Qiangtang terrane; (b) the mean inclinations calculated from the Jurassic, Cretaceous and Cenozoic palaeopoles, respectively; (c and d) plots of the mean ChRM directions of previous palaeomagnetic studies (declination and palaeolatitude, respectively). The solid black line represents the expected declination and palaeolatitude determined from the APWP curve of Eurasia (Besse & Courtillot. 2002, 2003). All these results have been converted to the reference point (32.5°N, 95.2°E). The red dashed box represents the possible timing of the remagnetization. The orange dashed box represents the time interval of the Cretaceous Normal Superchron (CNS).

Downloaded from https://academic.oup.com/gji/article/228/3/2073/6381694 by Vakgroep Wiskunde /University Library Utrecht user on 05 January 2022

Table 2. Palaeomagnetic poles for the Eastern Qiangtang Terrane.

Sampling site			Lithology	Age (Ma)	*N*(*n*)	Pole location			At reference position (32.5°N, 95.2°E)					Criteria (*Q*)	References
Location	Slat (°N)	Slon (°E)				Plat (°N)	Plon (°E)	A_{95} (°)	Palaeolat (°)	Dec (°)	ΔDec (°)	Inc (°)	ΔInc (°)		
Eastern Qiangtang Terrane															
Yanshiping	33.6	92.1	Clastic	165.5–171.2	25(182)	79.1	306.9	5	23.1 ± 5.3	−6.2	5.4	40	6.8	123□5R7(6)	Yan *et al.* (2016)
Yanshiping	33.6	92.1	Limestone	163.3–165.5	27(245)	68.9	313.8	2.8	15.3 ± 3.4	− 14	2.9	29	4.6	123F5R7(7)	Yan *et al.* (2016)
Yanshiping	33.6	92	Limestone	163.3–165.5	30(171)	65.5	335	7.8	18.2 ± 9.1	− 22	8.2	33	12.1	123□5□7(5)	Ren *et al.* (2013)
Zaduo	32.5	95.2	Limestone	163.3–165.5	12(123)	59.8	202.7	2.8	19.7 ± 2.8	31	3	36	4.2	123□5R7(6)	This study
Yanshiping	33.6	92.1	Sandstone	160.1–163.3	24(224)	66.1	332.1	3.5	17.7 ± 4.1	− 21	3.7	33	5.5	123F5R7(7)	Yan *et al.* (2016)
Yanshiping	33.6	92.1	Shale	157.5–160.1	20(191)	72.4	318.6	4.9	19.1 ± 5.6	− 13	5.2	35	7.4	123F5R7(7)	Yan *et al.* (2016)
Yanshiping	33.6	92.1	Limestone	157.5–160.1	6(59)	83.3	268.3	7.6	25.8 ± 7.7	0.9	8.4	44	9.7	123 F5□7(6)	Cheng *et al.* (2012)
Mangkang	29.7	98.4	Red beds	Berriasian-Barremian	12(68)	40.6	170.5	12	30.8 ± 10.9	59	13.9	50	13.3	123F5D7(7)	Huang *et al.* (1992)
Mangkang	29.7	98.7	Red beds	Aptian-Turonian	11(79)	56.7	172.7	9.5	33.3 ± 8.3	40	11.4	53	10	123F5□7(6)	Huang *et al.* (1992)
Mangkang	29.7	98.5	Red beds	K_2	17(186)	47	165.1	7.9	36.2 ± 6.5	53	9.8	56	7.7	□23F5R7(6)	Tong *et al.* (2015)
Gongjue	30.9	98.3	Sandstone	55.4–61	−(104)	43.4	181.2	3.8	24.3 ± 3.9	53	4.2	42	5	123F5R7(7)	Li *et al.* (2020)
Gongjue	30.9	98.3	Sandstone	53.2–55.4	−(68)	46.6	179.7	4.7	26.5 ± 4.7	50	6.3	45	5.9	123F5R7(7)	Li *et al.* (2020)
Xialaxiu	32.6	96.6	Volcanic rocks	49–51	21(−)	76.4	223.2	7.6	23.9 ± 7.6	12	8.3	41	10.3	123□5□□(4)	Roperch *et al.* (2017)
Gongjue	31	98.2	Red beds	43.2–56	43(−)	57.9	192.1	2.9	23.7 ± 3.1	35	3.2	41	3.9	123F5R7(7)	Tong *et al.* (2017)
Gongjue	31	98.2	Red beds	43–53	28(150)	55.1	216.2	2.2	11.1 ± 2.9	30	2.2	21	4	123F5R7(7)	Zhang *et al.* (2018)
Gongjue	31	98.2	Red beds	43–53	33(178)	65.5	237.8	2.4	12.2 ± 3.1	15	2.5	23	4.2	123F5R7(7)	Zhang *et al.* (2018)
Nangqian	32.2	96.6	Sandstone & Marlite	41–53	−(300)	71.7	190.5	4.5	29.1 ± 4.3	21	5.1	48	5.3	123□5R7(6)	Zhang *et al.* (2020a)
Gongjue	30.9	98.3	Sandstone	45.3–47.1	−(162)	60.8	181.5	2.9	29.7 ± 2.7	34	3.3	49	3.3	123F5R7(7)	Li *et al.* (2020)
Gongjue	30.9	98.3	Sandstone	41.5–45.3	−(196)	63.9	186	2.8	28.5 ± 2.7	30	3.2	47	3.3	123F5R7(7)	Li *et al.* (2020)
Wulanwula hu	34.5	90.2	Volcanic rocks	38.6 ± 0.5	7(53)	82.1	298.4	7.8	25.2 ± 8.0	−3.4	8.6	43	10.1	123F5□7(6)	Lippert *et al.* (2011)
Nangqian	32.2	96.6	Mudstone	35–41	−(267)	83.4	217.9	5.3	28.8 ± 5.0	6.3	6	48	6.3	123□5R7(6)	Zhang *et al.* (2020a)

Notes: Slat and Slon, latitude and longitude of the sampling site; Age (Ma), age of the rock units; *N*(*n*), number of sites (samples) used to calculate Fisherian mean; Plat. and Plon., latitude and longitude of the pole; A_{95}, radius of the 95 per cent confidence circle; Palaeolat, palaeolatitude calculated in respect to the reference site at 32.5°N, 95.2°E; Dec, ΔDec, Inc and ΔInc, declination and Inclination with their error converted to the reference site at 32.5°N, 95.2°E; Criteria (*Q*) = data quality criteria (number of criteria met) modified from Van der Voo (1990): 1, well-determined rock age; 2, sufficient number of samples ($N \geq 6$ and $n \geq 36$); 3, stepwise demagnetization; 4, robust field tests, F means positive fold test; 5, structural control and tectonic coherence with the craton or terrane discussed; 6, presence of reversal, R means positive reversal test and D means dual-polarity ChRM direction; 7, no resemblance to palaeopole of younger age (by more than a period); '□' in the criterion column fails to fulfill this criterion; Grey data are those failed to fulfill the criteria mentioned in the text.

Downloaded from https://academic.oup.com/gji/article/228/3/2073/6381694 by Vakgroep Wiskunde /University Library Utrecht user on 05 January 2022

overall structural trend turns from east–west-oriented in the central Tibetan Plateau to north–south-oriented in the southeastern edge of the Tibetan Plateau (Fig. 1). Zhang *et al.* (2020a) suggest that the Nangqian Basin has experienced a counterclockwise rotation of 25.9° ± 7.2° during ∼52–46 Ma, and an insignificant rotation during ∼46–41 Ma, followed by a clockwise rotation of 24.4° ± 9.7° during ∼41–35 Ma. Palaeomagnetic results of the Xialaxiu Basin volcanic rocks aged ∼49–51 Ma show a consistent declination as the nearby Nangqian Basin, which indicates similar rotation histories of these regions (Roperch *et al*. 2017). In the Gongjue Basin, a three-stage rotation history since ∼53 Ma is recorded as well (Zhang *et al*. 2018; Li *et al*. 2020). The Mangkang Basin underwent a clockwise rotation of ∼40° after the upper Cretaceous (Otofuji *et al*. 1990; Tong *et al*. 2015). Although the rotations vary with age, they are all clockwise which is noteworthy. Therefore, we believe that the ∼30° clockwise rotation of the Zaduo area is most likely due to the large-scale tectonic deformation of the eastern Tibetan Plateau after the India–Eurasia collision rather than a local deformation feature.

6.3. Mechanisms for the remagnetization of the Jurassic limestones

Thermoviscous resetting of existing magnetic minerals (Kent & Opdyke 1985) and chemical remanent magnetization (CRM) through magnetic mineral growth associated with orogenic fluids (e.g. Jackson 1990; Elmore *et al*. 2006, 2012; Huang *et al*. 2015, 2017a, b) currently are the most common mechanisms to explain remagnetization. The maximum burial temperature of the Buqu Formation was below 150 °C (Sun *et al*. 2020; Wu *et al*. 2020). However, the unblocking temperatures of the Jurrasic limestones in the study area are around 400–500 °C, giving a burial temperature of 150–350 °C based on the relaxation time-blocking temperature relationship for magnetite of Pullaiah *et al*. (1975). A lower burial temperature of below ∼200 °C would be obtained based on Kent's (1985).The remagnetization therefore could not be attributed to mere heating during burial. In addition, no Cenozoic igneous bodies are found near the section, but just Early Cretaceous intrusive rocks. Thermoviscous resetting is deemed a less likely mechanism for the remagnetization: it is hard to envisage that the intrusive rocks would have thermally reset the Jurassic limestones, but not nearby Permo-Triassic volcanic rocks (Guan *et al*. 2021). In fact, the rocks perhaps have not been heated for a sufficient amount of time at a sufficiently elevated temperature to make the thermal resetting feasible.

SSD magnetite with cogenetic SP particles is dominant magnetic carriers in the studied rocks. This authigenic magnetite may well be responsible for chemical remagnetization of many carbonate rocks (Suk *et al*. 1990a, 1990b; Morris & Robertson 1993; Jackson & Swanson-Hysell 2012; Huang *et al*. 2015, 2017a, b; Ran *et al*. 2017; Zhang *et al*. 2020b). Authigenic magnetite can be an oxidation product of iron sulfides (i.e. pyrite, pyrrhotite or greigite) under the influence of orogenic fluids (Reynolds 1990; Suk *et al*. 1990a; Roberts *et al*. 2011; Huang *et al*. 2015). To better understand this process, we recapitulate how organic matter diagenesis affects the formation of magnetic minerals that are typically preserved in carbonates.

Diagenesis involving degradation of organic matter after deposition is an essential process in the preservation of magnetic minerals in sedimentary environments. Microbes derive energy through uptake of oxygen and release of CO_2 from the organic matter. In general, consumption of the organic matter and accompanying respiration processes (in parentheses) are: oxic (aerobic respiration), nitrogenous (nitrate reduction), manganous (manganese reduction), ferruginous (iron reduction), sulphidic (sulphate reduction) and methanic (methanogenesis, Froelich *et al*. 1979; Roberts *et al*. 2013; Roberts 2015; Huang *et al*. 2019a). When one oxidant is used up, the next one will be used, until either all oxidants or all organic matter is consumed. This process is accompanied by the increase of dissolved Mn^{2+}, Fe^{2+} and HS^-. The Buqu Formation limestones were deposited in a littoral and shallow sea carbonate environment (Li *et al*. 2002; Tan *et al*. 2004; QGSI 2014; Yan *et al*. 2016; Cao *et al*. 2019). The appearance of massive bioclastic layers indicates that the climate was warm at that time, which was conducive to biological growth (QGSI 2014). Under those circumstances, organic carbon fluxes were high and anoxic sulphidic diagenetic environments were typically formed, in which paramagnetic pyrite would replace originally present detrital magnetite and hematite. If the Fe^{2+} supply rate is higher than the HS^- production, intermediate iron sulphides would be preserved (Kao *et al*. 2004; Roberts *et al*. 2013; Roberts 2015). In brief, the deposited sediments tend to undergo anoxic diagenesis and iron sulphides appear to be mainly formed during burial and diagenesis. After the India–Eurasia collision, the Nangqian, Gongjue and Mangkang basins have been uplifted to a fairly high elevation during Palaeogene (Su *et al*. 2019; Xu *et al*. 2013; Xiong *et al*. 2020). The diagenetic environment therefore turned from anoxic to suboxic and/or oxic, giving rise to oxidation of iron sulphide to authigenic magnetite and the acquisition of CRM (Brothers *et al*. 1996). This was likely mediated by the migration of orogenic fluids, fully endorsed by the occurrence of widespread gypsum veins in the Buqu Formation limestones (Gustavson *et al*. 1994; Philipp 2008; Bons *et al*. 2012; Gale *et al*. 2014). Two peaks of hydrocarbon generation occurred during the Early Cretaceous and Palaeogene, respectively (Wu *et al*. 2020). Fluids associated with hydrocarbon generation could be another trigger of remagnetization (e.g. Elmore *et al*. 2006, 2012), however, both phenomena probably worked in tandem (they operated at the same time). The nearby Permo-Triassic volcanic rocks as described in Guan *et al*. (2021) have a substantially lower porosity than the limestones, which avoids the circulation of orogenic fluids amid. In addition, the absence of organic matter in volcanic rocks does not drive reactions. Thus, the primary NRM has been retained in those rocks.

7. CONCLUSIONS

We report new palaeomagnetic results from limestones of the Middle to Late Callovian Buqu Formation in the Zaduo area, located in the eastern part of the Qiangtang Terrane. The primary NRM was overprinted by a CRM after the India–Eurasia collision. Rather uncommon in remagnetized strata, the secondary NRM dating from the Eocene has a 'false positive' reversals test. Due to the high organic carbon fluxes since the deposition of the Jurassic limestones, the oxygen was used up and the deposited sediments tend to be anoxic, thus iron sulphides appear to be mainly formed during burial and diagenesis. When the limestones were uplifted after the India–Eurasia collision, the diagenetic environment turned from anoxic to suboxic and/or oxic, giving rise to the oxidation of the pre-existing iron sulphides to authigenic magnetite and the acquisition of CRM. Like in many remagnetized limestones, the authigenic magnetite grains range from the superparamagnetic up to stable single-domain size, leading to distinctive rock-magnetic properties.

Downloaded from https://academic.oup.com/gji/article/228/3/2073/6381694 by Vakgroep Wiskunde /University Library Utrecht user on 05 January 2022

The remagnetization process is also manifested by the widespread occurrence of gypsum veins in the limestones. The secondary remanence reveals that the Zaduo area of the Eastern Qiangtang Terrane has experienced ∼15.7° ± 3.2° (∼1740 ± 350 km) of latitudinal crustal shortening since the Eocene. Besides, the ∼20° clockwise rotation of the Zaduo area relative to Eurasia coincides with the rotation pattern in the eastern part of the Qiangtang Terrane, indicating that the clockwise rotation accommodating the India–Eurasia collision was also prevailing in the Zaduo area.

ACKNOWLEDGEMENTS

This work was co-supported by the the Second Tibetan Plateau Scientific Expedition Program (Grant 2019QZKK0707), the Strategic Priority Research Program of Chinese Academy of Sciences (Grant XDA20070201), the Natural Science Foundation of China (Grants 41974080 and 41804065), the Basic Science Center for Tibetan Plateau Earth System (CTPES, Grant 41988101-01), and China Scholarship Council. The authors thank Weilin Zhang, Jinbo Zan, Tao Zhang, Yi Chen, Zengguang Guo, Mengqi Tan, Liye Yang, Yaofei Chen, and Zhongyu Xiong for their assistance in the laboratory work. We sincerely thank Editor Eduard Petrovsky, Assistant Editor Fern Storey, Professor Richard Elmore and another anonymous reviewer for their insightful comments and suggestions that greatly improved this paper.

DATA AVAILABILITY STATEMENT

The data underlying this paper are available in the paper and in its online supplementary material (https://doi.org/10.1093/gji/ggab402).

CONFLICT OF INTEREST

The authors acknowledge that there are no conflicts of interest recorded.

REFERENCES

Appel, E., Crouzet, C. & Schill, E., 2012. Pyrrhotite remagnetizations in the Himalaya: a review, *Geol. Soc., Lond., Spec. Publ.,* **371,** 163–180.

Besse, J. & Courtillot, V., 2002. Apparent and true polar wander and the geometry of the geomagnetic field over the last 200 Myr, *J. geophys. Res.,* **107,** EPM 6–1-EPM 6-31.

Besse, J. & Courtillot, V., 2003. Correction to "Apparent and true polar wander and the geometry of the geomagnetic field over the last 200 Myr", *J. geophys. Res.,* **108**(B10), doi:10.1029/2003JB002684.

Bian, W., Yang, T., Ma, Y., Jin, J., Gao, F., Zhang, S., Wu, H. & Li, H., 2017. New Early Cretaceous palaeomagnetic and geochronological results from the far western Lhasa terrane: contributions to the Lhasa-Qiangtang collision, *Sci. Rep.,* **7,** 1–14.

Bons, P.D., Elburg, M.A. & Gomez-Rivas, E., 2012. A review of the formation of tectonic veins and their microstructures, *J. Struct. Geol.,* **43,** 33–62.

Brothers, L., Engel, M. & Elmore, R., 1996. The late diagenetic conversion of pyrite to magnetite by organically complexed ferric iron, *Chem. Geol.,* **130,** 1–14.

Butler, R.F., 1992. *Paleomagnetism: Magnetic Domains to Geologic Terranes,* Vol. **319,** Blackwell Scientific Publications Boston, pp. 64–65.

Cao, Y. *et al.*, 2019. New paleomagnetic results from Middle Jurassic limestones of the Qiangtang terrane, Tibet: constraints on the evolution of the Bangong-Nujiang Ocean, *Tectonics,* **38,** 215–232.

Cao, Y. *et al.*, 2020. Paleomagnetism and U-Pb geochronology of early Cretaceous volcanic rocks from the Qiangtang Block, Tibetan Plateau: implications for the Qiangtang-Lhasa collision, *Tectonophysics,* **789,** doi:10.1016/j.tecto.2020.228500.

Chen, W. *et al.*, 2017. Combined paleomagnetic and geochronological study on Cretaceous strata of the Qiangtang terrane, central Tibet, *Gondwana Res.,* **41,** 373–389.

Chen, Y., Cogné, J. P., Courtillot, V., Tapponnier, P. & Zhu, X., 1993. Cretaceous paleomagnetic results from western Tibet and tectonic implications, *J. geophys. Res.,* (**98**), 17981–17999.

Chen, Y., Ding, L., Li, Z., Laskowski, A.K., Li, J., Baral, U., Qasim, M. & Yue, Y., 2020. Provenance analysis of Cretaceous peripheral foreland basin in central Tibet: implications to precise timing on the initial Lhasa-Qiangtang collision, *Tectonophysics,* **775,** 228311, doi:10.1016/j.tecto.2019.228311.

Cheng, X. *et al.*, 2012. New paleomagnetic result of the Middle-Late Jurassic rocks from northern Qiangtang Block, west China, *Chinese J. Geophys.,* **55,** 3399–3409.

Cogné, J., Halim, N., Chen, Y. & Courtillot, V., 1999. Resolving the problem of shallow magnetizations of Tertiary age in Asia: insights from paleomagnetic data from the Qiangtang, Kunlun, and Qaidam blocks (Tibet, China), and a new hypothesis, *J. geophys. Res.,* **104,** 17 715–17 734.

Dekkers, M. & Pietersen, H.S., 1991. Magnetic properties of low-Ca fly ash: a rapid tool for Fe-assessment and a survey for potentially hazardous elements, *MRS Online Proc. Library,* **245,** 37–47.

Dewey, J.F., Cande, S. & Pitman, W.C., 1989. Tectonic evolution of the India/Eurasia collision zone, *Eclogae Geol. Helv.,* **82,** 717–734.

Dewey, J.F., Shackleton, R.M., Chengfa, C. & Yiyin, S., 1988. The tectonic evolution of the Tibetan Plateau, *Phil. Trans. R. Soc. Lond., A,* **327,** 379–413.

Ding, L. *et al.*, 2017. Processes of initial collision and suturing between India and Asia, *Sci. China Earth Sci.,* **60,** 635–651.

Ding, L., Kapp, P. & Wan, X., 2005. Paleocene–Eocene record of ophiolite obduction and initial India-Asia collision, south central Tibet, *Tectonics,* **24,** doi:10.1029/2004TC001729.

Dong, X., Wang, Z., Tan, C., Yang, H., Cheng, L. & Zhou, Y., 1990. New paleomagnetic results from Yadong-Golmud geoscience transect and a preliminary study on the model of terranes evolution in Qinghai-Xizang Plateau, *Chin. Acad. Geol. Sci.,* **21,** 139–148.

Dong, X., Wang, Z., Tan, C., Yang, H., Cheng, L. & Zhou, Y., 1991. New results of paleomagnetic studies of the Qinghai-Tibetan plateau, *Geol. Rev.,* **37,** 160–164.

Douglas Elmore, R., Lee-Egger Foucher, J., Evans, M., Lewchuk, M. & Cox, E., 2006. Remagnetization of the Tonoloway formation and the Helderberg Group in the Central Appalachians: testing the origin of syntilting magnetizations, *Geophys. J. Int.,* **166,** 1062–1076.

Dunlop, D.J., 2002. Theory and application of the Day plot (Mrs/Ms versus Hcr/Hc) 2. Application to data for rocks, sediments, and soils, *J. geophys. Res.,* **107,** EPM 5–1-EPM 5-15.

Dupont-Nivet, G., Lippert, P.C., Van Hinsbergen, D.J., Meijers, M.J. & Kapp, P., 2010a. Palaeolatitude and age of the Indo–Asia collision: palaeomagnetic constraints, *Geophys. J. Int.,* **182,** 1189–1198.

Dupont-Nivet, G., Van Hinsbergen, D.J. & Torsvik, T.H., 2010b. Persistently low Asian paleolatitudes: implications for the India-Asia collision history, *Tectonics,* **29**(5), doi:10.1029/2008TC002437.

Egli, R., 2004. Characterization of individual rock magnetic components by analysis of remanence curves, 1. Unmixing natural sediments, *Stud. Geophys. Geod.,* **48,** 391–446.

Elmore, R.D., Muxworthy, A.R. & Aldana, M., 2012. Remagnetization and chemical alteration of sedimentary rocks, *Geol. Soc., Lond., Spec. Publ.,* **371,** 1–21.

Fan, J, Li, C., Xie, C., Wang, M. & Chen, J., 2015. The evolution of the Bangong–Nujiang Neo-Tethys ocean: evidence from zircon U–Pb and Lu–Hf isotopic analyses of Early Cretaceous oceanic islands and ophiolites, *Tectonophysics,* **655,** 27–40.

Fan, J., Li, C., Liu, J., Wang, M., Liu, Y. & Xie, C., 2018a. The Middle Triassic evolution of the Bangong–Nujiang Tethyan Ocean: evidence from analyses of OIB-type basalts and OIB-derived phonolites in northern Tibet, *Int. J. Earth Sci.,* **107,** 1755–1775.

Downloaded from https://academic.oup.com/gji/article/228/3/2073/6381694 by Vakgroep Wiskunde /University Library Utrecht user on 05 January 2022

Fan, J., Li, C., Wang, M. & Xie, C., 2018b. Reconstructing in space and time the closure of the middle and western segments of the Bangong–Nujiang Tethyan Ocean in the Tibetan Plateau, *Int. J. Earth Sci.,* **107,** 231–249.

Fan, J., Li, C., Xie, C. & Wang, M., 2014. Petrology, geochemistry, and geochronology of the Zhonggang ocean island, northern Tibet: implications for the evolution of the Banggongco–Nujiang oceanic arm of the Neo-Tethys, *Int. Geol. Rev.,* **56,** 1504–1520.

Fang, X. *et al.*, 2016. Mesozoic litho-and magneto-stratigraphic evidence from the central Tibetan Plateau for megamonsoon evolution and potential evaporites, *Gondwana Res.,* **37,** 110–129.

Fisher, R.A., 1953. Dispersion on a sphere, *Proc. R. Soc. Lond., A.,* **217,** 295–305.

Froelich, P.N. *et al.*, 1979. Early oxidation of organic matter in pelagic sediments of the eastern equatorial Atlantic: suboxic diagenesis, *Geochim. cosmochim. Acta.,* **43,** 1075–1090.

Gale, A., Mutterlose, J., Batenburg, S., Gradstein, F., Agterberg, F., Ogg, J. & Petrizzo, M., 2020. The Cretaceous period, in *Geologic Time Scale 2020,* pp. 1023–1086.

Gale, J.F., Laubach, S.E., Olson, J.E., Eichhubl, P. & Fall, A., 2014. Natural fractures in shale: a review and new observations natural fractures in shale: a review and new observations, *AAPG Bull.,* **98,** 2165–2216.

Gao, L., Yang, Z., Han, Z., Tong, Y., Jing, X. & Zhang, S.-H., 2018. Remagnetization of the Lower Ordovician Hongshiya Formation of the southwestern Yangtze Block, *Tectonophysics,* **738,** 83–91.

Ge, K., Liu, Q., Deng, J., D. Nobes, Wang, Y., Wang, Y. & Chen, X., 2017. Rock magnetic investigation and its geological significance for vein-type uranium deposits in southern China, *Geochem, Geophys, Geosyst,* **18,** 1333–1349.

Gong, Z., Dekkers, M., Heslop, D. & Mullender, T., 2009. End-member modelling of isothermal remanent magnetization (IRM) acquisition curves: a novel approach to diagnose remagnetization, *Geophys. J. Int.,* **178,** 693–701.

Guan, C. *et al.*, 2021. Paleomagnetic and chronologic data bearing on the Permian/Triassic boundary position of Qamdo in the Eastern Qiantang Terrane: implications for the Closure of the Paleo-Tethys, *Geophys. Res. Lett.,* **48**(6), e2020GL092059, doi:10.1029/2020GL092059.

Gustavson, T.C., Hovorka, S.D. & Dutton, A.R., 1994. Origin of satin spar veins in evaporite basins, *J. Sediment. Res.,* **64,** 88–94.

Heslop, D., McIntosh, G. & Dekkers, M., 2004. Using time-and temperature-dependent Preisach models to investigate the limitations of modelling isothermal remanent magnetization acquisition curves with cumulative log Gaussian functions, *Geophys. J. Int.,* **157,** 55–63.

Huang, K. & Opdyke, N.D., 2015. Post-folding magnetization of the Triassic rocks from western Guizhou and southern Yunnan provinces: new evidence for large clockwise rotations in the Simao Terrane, *Earth planet. Sci. Lett.,* **423,** 155–163.

Huang, K., Opdyke, N.D., Li, J. & Peng, X., 1992. Paleomagnetism of Cretaceous rocks from eastern Qiangtang terrane of Tibet, *J. geophys. Res.,* **97,** 1789–1799.

Huang, W. *et al.*, 2015. Paleolatitudes of the T ibetan H imalaya from primary and secondary magnetizations of Jurassic to Lower Cretaceous sedimentary rocks, *Geochem. Geophys. Geosyst.,* **16,** 77–100.

Huang, W. *et al.*, 2017a. Remagnetization of the Paleogene Tibetan Himalayan carbonate rocks in the Gamba area: implications for reconstructing the lower plate in the India-Asia collision, *J. geophys. Res.,* **122,** 808–825.

Huang, W. *et al.*, 2017b. Remagnetization of carbonate rocks in southern Tibet: perspectives from rock magnetic and petrographic investigations, *J. geophys. Res.,* **122,** 2434–2456.

Huang, W., Jackson, M.J., Dekkers, M.J., Solheid, P., Zhang, B., Guo, Z. & Ding, L., 2019a. Nanogoethite as a potential indicator of remagnetization in red beds, *Geophys. Res. Lett.,* **46,** 12841–12850.

Huang, W., Jackson, M.J., Dekkers, M.J., Zhang, Y., Zhang, B., Guo, Z. & Dupont-Nivet, G., 2019b. Challenges in isolating primary remanent magnetization from Tethyan carbonate rocks on the Tibetan Plateau: insight from remagnetized Upper Triassic limestones in the eastern Qiangtang block, *Earth planet. Sci. Lett.,* **523,** 115695.

Jackson, M., 1990. Diagenetic sources of stable remanence in remagnetized Paleozoic cratonic carbonates: a rock magnetic study, *J. geophys. Res.,* **95,** 2753–2761.

Jackson, M., Rochette, P., Fillion, G., Banerjee, S. & Marvin, J., 1993. Rock magnetism of remagnetized Paleozoic carbonates: low-temperature behavior and susceptibility characteristics, *J. geophys. Res.,* **98,** 6217–6225.

Jackson, M. & Swanson-Hysell, N.L., 2012. Rock magnetism of remagnetized carbonate rocks: another look, *Geol. Soc., Lond., Spec. Publ.,* **371,** 229–251.

Kao, S., Horng, C., Roberts, A.P. & Liu, K., 2004. Carbon–sulfur–iron relationships in sedimentary rocks from southwestern Taiwan: influence of geochemical environment on greigite and pyrrhotite formation, *Chem. Geol.,* **203,** 153–168.

Kapp, P., DeCelles, P.G., Gehrels, G.E., Heizler, M. & Ding, L., 2007. Geological records of the Lhasa-Qiangtang and Indo-Asian collisions in the Nima area of central Tibet, *Bull. geol. Soc. Am.,* **119,** 917–933.

Kapp, P., Murphy, M.A., Yin, A., Harrison, T.M., Ding, L. & Guo, J., 2003. Mesozoic and Cenozoic tectonic evolution of the Shiquanhe area of western Tibet, *Tectonics,* **22**(4), doi:10.1029/2001TC001332.

Kent, D.V., 1985. Thermoviscous remagnetization in some Appalachian limestones, *Geophys. Res. Lett.,* **12,** 805–808.

Kent, D.V. & Opdyke, N.D., 1985. Multicomponent magnetizations from the Mississippian Mauch Chunk Formation of the central Appalachians and their tectonic implications, *J. geophys. Res.,* **90,** 5371–5383.

Kirschvink, J., 1980. The least-squares line and plane and the analysis of palaeomagnetic data, *Geophys. J. Int.,* **62,** 699–718.

Kruiver, P.P., Dekkers, M.J. & Heslop, D., 2001. Quantification of magnetic coercivity components by the analysis of acquisition curves of isothermal remanent magnetisation, *Earth planet. Sci. Lett.,* **189,** 269–276.

Li, B. *et al.*, 2017a. New paleomagnetic constraints on middle Miocene strike-slip faulting along the middle Altyn Tagh Fault, *J. geophys. Res.,* **122,** 4106–4122.

Li, C., Zhai, G., Wang, L., Yin, F. & Mao, X., 2009. An important window for understanding the Qinghai–Tibet Plateau—a review on research progress in recent years of Qiangtang area, Tibet, China, *Geological Bulletin of China,* **28,** 1169–1177.

Li, S. *et al.*, 2017b. Clockwise rotations recorded in redbeds from the Jinggu Basin of northwestern Indochina, *Bull. geol. Soc. Am.,* **129,** 1100–1122.

Li, S., Guilmette, C., Yin, C., Ding, L., Zhang, J., Wang, H. & Baral, U., 2019a. Timing and mechanism of Bangong-Nujiang ophiolite emplacement in the Gerze area of central Tibet, *Gondwana Res.,* **71,** 179–193.

Li, S., van Hinsbergen, D.J., Najman, Y., Liu, Z., Deng, C. & Zhu, R., 2020. Does pulsed Tibetan deformation correlate with Indian plate motion changes?, *Earth planet. Sci. Lett.,* **536,** 116144.

Li, S., Yin, C., Guilmette, C., Ding, L. & Zhang, J., 2019b. Birth and demise of the Bangong-Nujiang Tethyan Ocean: a review from the Gerze area of central Tibet, *Earth Sci. Rev.,* **198,** 102907.

Li, Y., Wang, C. & Yi, H., 2002. Filled sequence and evolution of the Mesozoic Qiangtang composite foreland basin in the Qinghai-Tibet Plateau, *Journal of Stratigraphy,* **26,** 62–67.

Li, Z., Ding, L., Song, P., Fu, J. & Yue, Y., 2017c. Paleomagnetic constraints on the paleolatitude of the Lhasa block during the Early Cretaceous: implications for the onset of India–Asia collision and latitudinal shortening estimates across Tibet and stable Asia, *Gondwana Res.,* **41,** 352–372.

Liebke, U., Appel, E., Ding, L. & Zhang, Q., 2013. Age constraints on the India–Asia collision derived from secondary remanences of Tethyan Himalayan sediments from the Tingri area, *J. Asian Earth Sci.,* **62,** 329–340.

Lin, J. & Watts, D., 1988. Palaeomagnetic results from the Tibetan Plateau, *Phil. Trans. R. Soc. Lond., A,* **327,** 239–262.

Lippert, P.C., Zhao, X., Coe, R.S. & Lo, C.-H., 2011. Palaeomagnetism and 40Ar/39Ar geochronology of upper Palaeogene volcanic rocks from Central Tibet: implications for the Central Asia inclination anomaly, the palaeolatitude of Tibet and post-50 Ma shortening within Asia, *Geophys. J. Int.,* **184,** 131–161.

Downloaded from https://academic.oup.com/gji/article/228/3/2073/6381694 by Vakgroep Wiskunde /University Library Utrecht user on 05 January 2022

Liu, C., Li, S., Deng, C. & Zhu, R., 2013. On the mechanism of remagnetization of Ordovician carbonates from the Yangtze Block, southwestern China, *Chinese J. Geophys.,* **56,** 579–591.

Liu, D., Huang, Q., Fan, S., Zhang, L., Shi, R. & Ding, L., 2014. Subduction of the Bangong–Nujiang Ocean: constraints from granites in the Bangong Co area, Tibet, *Geol. J.,* **49,** 188–206.

Lowrie, W., 1990. Identification of ferromagnetic minerals in a rock by coercivity and unblocking temperature properties, *Geophys. Res. Lett.,* **17,** 159–162.

Ma, A., Hu, X., Garzanti, E., Han, Z. & Lai, W., 2017. Sedimentary and tectonic evolution of the southern Qiangtang basin: implications for the Lhasa-Qiangtang collision timing, *J. geophys. Res.,* **122,** 4790–4813.

Ma, Y. *et al.*, 2014. Paleomagnetism and U-Pb zircon geochronology of Lower Cretaceous lava flows from the western Lhasa terrane: new constraints on the India-Asia collision process and intracontinental deformation within Asia, *J. geophys. Res.,* **119,** 7404–7424.

McCabe, C. & Channell, J., 1994. Late Paleozoic remagnetization in limestones of the Craven Basin (northern England) and the rock magnetic fingerprint of remagnetized sedimentary carbonates, *J. geophys. Res.,* **99,** 4603–4612.

McFadden, P. & McElhinny, M., 1990. Classification of the reversal test in palaeomagnetism, *Geophys. J. Int.,* **103,** 725–729.

Meert, J.G. *et al.*, 2020. The magnificent seven: a proposal for modest revision of the quality index, *Tectonophysics,* **790,** 228549.

Meijers, M.J., Van Hinsbergen, D.J., Dekkers, M.J., Altıner, D., Kaymakcı, N. & Langereis, C.G., 2011. Pervasive Palaeogene remagnetization of the central Taurides fold-and-thrust belt (southern Turkey) and implications for rotations in the Isparta Angle, *Geophys. J. Int.,* **184,** 1090–1112.

Meng, J., Zhao, X., Wang, C., Liu, H., Li, Y., Han, Z., Liu, T. & Wang, M., 2018. Palaeomagnetism and detrital zircon U–Pb geochronology of Cretaceous redbeds from central Tibet and tectonic implications, *Geol. J.,* **53,** 2315–2333.

Metcalfe, I., 2013. Gondwana dispersion and Asian accretion: tectonic and palaeogeographic evolution of eastern Tethys, *J. Asian Earth Sci.,* **66,** 1–33.

Morris, A. & Robertson, A., 1993. Miocene remagnetisation of carbonate platform and Antalya Complex units within the Isparta Angle, SW Turkey, *Tectonophysics,* **220,** 243–266.

Otofuji, Y.-i., Inoue, Y., Funahara, S., Murata, F. & Zheng, X., 1990. Palaeomagnetic study of eastern Tibet-deformation of the Three Rivers region, *Geophys. J. Int.,* **103,** 85–94.

Pan, G., Ding, J., D. Yao & Wang, L., 2004. Guidebook of 1: 1,500,000 geologic map of the Qinghai–Xizang (Tibet) plateau and adjacent areas, Chengdu, China: Chengdu Cartographic Publishing House, 48.

Parnell, J., Baron, M., Davidson, M., Elmore, D. & Engel, M., 2000. Dolomitic breccia veins as evidence for extension and fluid flow in the Dalradian of Argyll, *Geol. Mag.,* **137,** 447–462.

Perroud, H. & Van der Voo, R., 1984. Secondary magnetizations from the Clinton-type iron ores of the Silurian Red Mountain Formation, Alabama, *Earth planet. Sci. Lett.,* **67,** 391–399.

Philipp, S.L., 2008. Geometry and formation of gypsum veins in mudstones at Watchet, Somerset, SW England, *Geol. Mag.,* **145,** 831–844.

Pike, C.R., Roberts, A.P. & Verosub, K.L., 2001. First order reversal curve diagrams and thermal relaxation effects in magnetic particles, *Geophys. J. Int.,* **145,** 721–730.

Pullaiah, G., Irving, E., Buchan, K. & Dunlop, D., 1975. Magnetization changes caused by burial and uplift, *Earth planet. Sci. Lett.,* **28,** 133–143.

Qin, H., Liu, Q. & Pan, Y., 2008. The first-order reversal curve (FORC) diagram: theory and case study, *Chinese J. Geophys.,* **51,** 743–751.

Qinghai Geological Survey Institute (QGSI). 2005. *Geological Map (1:250000) of the People's Republic of China-Zaduo County Sheet,* China University of Geosciences Press (In Chinese).

Qinghai Geological Survey Institute (QGSI). 2014. *1:250000 Geological Survey Report of the People's Republic of China-Zaduo County sheet*. China University of Geosciences Press (in Chinese). ISBN: 9787562533832.

Ran, B. *et al.*, 2017. Kinematics of the crust around the Tanggula Shan in North–Central Tibet: constraints from paleomagnetic data, *Gondwana Res.,* **48,** 124–133.

Ren, H., Yan, M., Meng, Q., Song, C. & Fang, X., 2013. E/I corrected paleomagnetic inclination indicates 1 000 km NS shortening of the Qiangtang terrane since the Middle Jurassic, *Chinese J. Geol.,* **48,** 543–556.

Reynolds, R.L., 1990. A polished view of remagnetization, *Nature,* **345,** 579–580.

Roberts, A.P., 2015. Magnetic mineral diagenesis, *Earth Sci. Rev.,* **151,** 1–47.

Roberts, A.P., Chang, L., Rowan, C.J., Horng, C.S. & Florindo, F., 2011. Magnetic properties of sedimentary greigite (Fe_3S_4): an update, *Rev. Geophys.,* **49,** RG1002.

Roberts, A.P., Cui, Y. & Verosub, K.L., 1995. Wasp-waisted hysteresis loops: mineral magnetic characteristics and discrimination of components in mixed magnetic systems, *J. geophys. Res.,* **100,** 17909–17924.

Roberts, A.P., Florindo, F., Chang, L., Heslop, D., Jovane, L. & Larrasoana, J.C., 2013. Magnetic properties of pelagic marine carbonates, *Earth Sci. Rev.,* **127,** 111–139.

Roberts, A.P., Heslop, D., Zhao, X. & Pike, C.R., 2014. Understanding fine magnetic particle systems through use of first-order reversal curve diagrams, *Rev. Geophys.,* **52,** 557–602.

Roberts, A.P., Liu, Q., Rowan, C.J., Chang, L., Carvallo, C., Torrent, J. & Horng, C.S., 2006. Characterization of hematite (α-Fe_2O_3), goethite (α-FeOOH), greigite (Fe_3S_4), and pyrrhotite (Fe_7S_8) using first-order reversal curve diagrams, *J. geophys. Res.,* **111,** B12, doi:10.1029/2006JB004715.

Roberts, A.P., Tauxe, L., Heslop, D., Zhao, X. & Jiang, Z., 2018. A critical appraisal of the "Day" diagram, *J. geophys. Res.,* **123,** 2618–2644.

Roger, F., Jolivet, M. & Malavieille, J., 2010. The tectonic evolution of the Songpan-Garzê (North Tibet) and adjacent areas from Proterozoic to Present: a synthesis, *J. Asian Earth Sci.,* **39,** 254–269.

Roperch, P. *et al.*, 2017. Paleomagnetic constraints on early collisional deformation along the eastern margin of the Qiantang terrane (Tibetan plateau) at 50 and 37 Ma, in *Proceedings of the 19th EGU General Assembly, EGU2017,* Abstracts, held 23-28 April, 2017 in Vienna, Austria, p. 9476.

Shen, M., Zan, J., Yan, M., Zhang, W., Fang, X., Zhang, D. & Zhang, T., 2020. Comparative rock magnetic study of Eocene volcanogenic and sedimentary rocks from Yunnan, southeastern Tibetan Plateau, and its geological implications, *J. geophys. Res.,* **125,** 2169–9313, 10.1029/2019JB017946.

Song, C., Wang, J., Fu, X., Feng, X., Chen, M. & He, L., 2012. Late Triassic paleomagnetic data from the Qiangtang terrane of Tibetan Plateau and their tectonic significances, *Journal of Jilin University (Earth Science Edition),* **42,** 241–250.

Song, C., Zeng, Y., Yan, M., Wu, S., Fang, X., Bao, J., Zan, J. & Liu, X., 2016. Magnetostratigraphy of the middle-upper Jurassic sedimentary sequences at Yanshiping, Qiangtang Basin, China, *Geophys. J. Int.,* **206,** 1847–1863.

Song, P., Ding, L., Li, Z., Lippert, P.C., Yang, T., Zhao, X., Fu, J. & Yue, Y., 2015. Late Triassic paleolatitude of the Qiangtang block: implications for the closure of the Paleo-Tethys Ocean, *Earth planet. Sci. Lett.,* **424,** 69–83.

Song, P., Ding, L., Lippert, P.C., Li, Z., Zhang, L. & Xie, J., 2020. Paleomagnetism of Middle Triassic lavas from northern Qiangtang (Tibet): constraints on the closure of the Paleo-Tethys Ocean, *J. geophys. Res.,* **125**(2), e2019JB017804, doi:10.1029/2019JB017804.

Su, T. *et al.*, 2019. Uplift, climate and biotic changes at the Eocene–Oligocene transition in south-eastern Tibet, *Natl. Sci. Rev.,* **6,** 495–504.

Suk, D., Peacor, D. & Van der Voo, R., 1990a. Replacement of pyrite framboids by magnetite in limestone and implications for palaeomagnetism, *Nature,* **345,** 611–613.

Suk, D., Van Der Voo, R. & Peacor, D.R., 1990b. Scanning and transmission electron microscope observations of magnetite and other iron phases in Ordovician carbonates from east Tennessee, *J. geophys. Res.,* **95,** 12 327–12 336.

Sun, W., Chen, M., Wan, Y., He, J., Lan, Y., Wei, H. & CHen, H. 2020. Closed-system dolomitization process and the significance for petroleum geology—an example from dolostone in the Middle Jurassic Buqu Formation in southern Qiangtang depression, *Geol. Rev.,* **66,** 1217–1229.

Downloaded from https://academic.oup.com/gji/article/228/3/2073/6381694 by Vakgroep Wiskunde /University Library Utrecht user on 05 January 2022

Tan, F., Wang, J., Li, Y., Du, B. & Zhu, Z., 2004. Late Jurassic–Early Cretaceous strata and their sedimentary characteristics in the Qiangtang basin, northern Tibet, *Geol. China,* **31,** 20–27.

Tan, X., Kodama, K.P., Chen, H., Fang, D., Sun, D. & Li, Y., 2003. Paleomagnetism and magnetic anisotropy of Cretaceous red beds from the Tarim basin, northwest China: evidence for a rock magnetic cause of anomalously shallow paleomagnetic inclinations from central Asia, *J. geophys. Res.,* **108**(B2), doi:10.1029/2001JB001608.

Tang, X., Huang, B., Yang, L., Yi, Z., Qiao, Q. & Chen, L., 2013. Paleomagnetism and Ar-Ar geochronology of Cretaceous volcanic rocks in the middle Lhasa terrane, China and tectonic implications, *Chinese J. Geophys.,* **56,** 136–149.

Tapponnier, P., Peltzer, G., Le Dain, A., Armijo, R. & Cobbold, P., 1982. Propagating extrusion tectonics in Asia: new insights from simple experiments with plasticine, *Geology,* **10,** 611–616.

Tapponnier, P., Zhiqin, X., Roger, F., Meyer, B., Arnaud, N., Wittlinger, G. & Jingsui, Y., 2001. Oblique stepwise rise and growth of the Tibet Plateau, *Science,* **294,** 1671–1677.

Tauxe, L. & Kent, D.V., 2004. A simplified statistical model for the geomagnetic field and the detection of shallow bias in paleomagnetic inclinations: was the ancient magnetic field dipolar?in *Timescales of the Palaeomagnetic Field,* pp. 101–117. eds Channell, J.E.T., Kent, D.V., Lowrie, W., Meert & J.G., Geophysical Monograph 145, American Geophysical Union.

Tauxe, L., Mullender, T. & Pick, T., 1996. Potbellies, wasp-waists, and superparamagnetism in magnetic hysteresis, *J. geophys. Res.,* **101,** 571–583.

Tong, Y., Yang, Z., Gao, L., Wang, H., Zhang, X., An, C., Xu, Y. & Han, Z., 2015. Paleomagnetism of Upper Cretaceous red-beds from the eastern Qiangtang Block: clockwise rotations and latitudinal translation during the India–Asia collision, *J. Asian Earth Sci.,* **114,** 732–749.

Tong, Y., Yang, Z., Mao, C., Pei, J., Pu, Z. & Xu, Y., 2017. Paleomagnetism of Eocene red-beds in the eastern part of the Qiangtang Terrane and its implications for uplift and southward crustal extrusion in the southeastern edge of the Tibetan Plateau, *Earth planet. Sci. Lett.,* **475,** 1–14.

Van der Voo, R., 1990. The reliability of paleomagnetic data, *Tectonophysics,* **184,** 1–9.

Van der Voo, R. & Torsvik, T.H., 2012. The history of remagnetization of sedimentary rocks: deceptions, developments and discoveries, *Geol. Soc., Lond., Spec. Publ.,* **371,** 23–53.

Van Hinsbergen, D.J., Lippert, P.C., Dupont-Nivet, G., McQuarrie, N., Doubrovine, P.V., Spakman, W. & Torsvik, T.H., 2012. Greater India Basin hypothesis and a two-stage Cenozoic collision between India and Asia, *Proc. Natl. Acad. Sci.,* **109,** 7659–7664.

Wu, Z., Ji, C., Zhao, Z. & Chen, C., 2020. Buried depth evolution and hydrocarbon generation history of the Jurassic System in central Qiangtang Basin. *Acta Geol. Sin.,* **94,** 102 823–102 833.

Xiong, Z. *et al.*, 2020. The early Eocene rise of the Gonjo Basin, SE Tibet: from low desert to high forest, *Earth planet. Sci. Lett.,* **543,** 116312.

Xu, Q., Ding, L., Zhang, L., Cai, F., Lai, Q., Yang, D. & Liu-Zeng, J., 2013. Paleogene high elevations in the Qiangtang Terrane, central Tibetan Plateau, *Earth planet. Sci. Lett.,* **362,** 31–42.

Xu, R., Schärer, U. & Allègre, C.J., 1985. Magmatism and metamorphism in the Lhasa block (Tibet): a geochronological study, *J. Geol.,* **93,** 41–57.

Xu, Y., Yang, Z., Tong, Y.-B., Wang, H., Gao, L. & An, C., 2015. Further paleomagnetic results for lower Permian basalts of the Baoshan Terrane, southwestern China, and paleogeographic implications, *J. Asian Earth Sci.,* **104,** 99–114.

Yan, M., Van der Voo, R., Tauxe, L., Fang, X. & Parés, M, J., 2005. Shallow bias in Neogene palaeomagnetic directions from the Guide Basin, NE Tibet, caused by inclination error, *Geophys. J. Int.,* **163,** 944–948.

Yan, M., Zhang, D., Fang, X., Ren, H., Zhang, W., Zan, J., Song, C. & Zhang, T., 2016. Paleomagnetic data bearing on the Mesozoic deformation of the Qiangtang Block: implications for the evolution of the Paleo-and Meso-Tethys, *Gondwana Res.,* **39,** 292–316.

Yin, A. & Harrison, T.M., 2000. Geologic evolution of the Himalayan-Tibetan orogen, *Annu. Rev. Earth Planet. Sci.,* **28,** 211–280.

Zegers, T., Dekkers, M. & Bailly, S., 2003. Late carboniferous to permian remagnetization of Devonian limestones in the Ardennes: role of temperature, fluids, and deformation, *J. geophys. Res.,* **108**(B7), 2357.

Zhang, D., Yan, M., Song, C., Zhang, W., Fang, X. & Li, B., 2021. Frequent polarity reversals in the cretaceous normal superchron, *Geophys. Res. Lett.,* **48**(5), e2020GL091501, doi:10.1029/2020GL091501.

Zhang, K., Zhang, Y., Tang, X. & Xia, B., 2012. Late Mesozoic tectonic evolution and growth of the Tibetan plateau prior to the Indo-Asian collision, *Earth Sci. Rev.,* **114,** 236–249.

Zhang, W., Fang, X., Zhang, T., Song, C. & Yan, M., 2020a. Eocene rotation of the northeastern central Tibetan Plateau indicating stepwise compressions and eastward extrusions, *Geophys. Res. Lett.,* **47**(17), e2020GL088989, doi:10.1029/2020GL088989.

Zhang, Y. *et al.*, 2020b. Fluid migration and widespread remagnetization in the Dabashan fold and thrust belt, China, *J. geophys. Res.,* **125,** e2020JB019989, doi:10.1029/2020JB019989.

Zhang, Y., Huang, W., Huang, B., van Hinsbergen, D.J., Yang, T., Dupont-Nivet, G. & Guo, Z., 2018. 53–43 Ma deformation of eastern Tibet revealed by three stages of tectonic rotation in the Gongjue basin, *J. geophys. Res.,* **123,** 3320–3338.

Zhou, Y. *et al.*, 2019. The northern Qiangtang Block rapid drift during the Triassic Period: paleomagnetic evidence, *Geosci. Front.,* **10,** 2313–2327.

Zhu, D., Li, S., Cawood, P.A., Wang, Q., Zhao, Z., Liu, S. & Wang, L., 2016. Assembly of the Lhasa and Qiangtang terranes in central Tibet by divergent double subduction, *Lithos,* **245,** 7–17.

Zhu, D., Pan, G., Mo, X., Wang, L., Zhao, Z., Liao, Z., Geng, Q. & Dong, G., 2006. Identification for the Mesozoic OIB-type basalts in central Qinghai-Tibetan Plateau: geochronology, geochemistry and their tectonic setting, *Acta Geol. Sin.,* **80,** 1312–1328.

Zhu, D., Zhao, Z., Niu, Y., Dilek, Y., Hou, Z. & Mo, X., 2013. The origin and pre-Cenozoic evolution of the Tibetan Plateau, *Gondwana Res.,* **23,** 1429–1454.

Zhu, D., Zhao, Z., Niu, Y., Mo, X., Chung, S., Hou, Z., Wang, L. & Wu, F., 2011. The Lhasa Terrane: record of a microcontinent and its histories of drift and growth, *Earth planet. Sci. Lett.,* **301,** 241–255.

Zwing, A., Clauer, N., Liewig, N. & Bachtadse, V., 2009. Identification of remagnetization processes in Paleozoic sedimentary rocks of the northeast Rhenish Massif in Germany by K-Ar dating and REE tracing of authigenic illite and Fe oxides, *J. geophys. Res.,* **114**(B6), doi:10.1029/2008JB006137.

SUPPORTING INFORMATION

Supplementary data are available at *GJIRAS* online.

Please note: Oxford University Press is not responsible for the content or functionality of any supporting materials supplied by the authors. Any queries (other than missing material) should be directed to the corresponding author for the paper.

Downloaded from https://academic.oup.com/gji/article/228/3/2073/6381694 by Vakgroep Wiskunde /University Library Utrecht user on 05 January 2022